RSC Advances

REVIEW

View Article Online
View Journal | View Issue

Cite this: *RSC Adv.*, 2025, **15**, 30654

Mesoporous zirconium based metal–organic frameworks, a topological review

Pouya Khattami Kermanshahi, Pooria Refah and Kamran Akhbari *

Through the gathering of metals and clusters with organic linkers, the metal–organic frameworks (MOFs) family emerges, representing highly applicable class of porous and crystalline materials in the world of chemistry. This class has the potential to shape the future of this field of science. The remarkable stability of zirconium and carboxylate ligands, coupled with the possibility of creating highly porous structures with a variety of arrangements, has led the authors to compile this review. In this study, we will investigate ten topologies that appeared in reported mesoporous Zr-Based MOFs and discuss their special properties. The applications of these structures are strongly influenced by their topologies, and the authors have concluded that understanding the topology and, more generally, the structure of MOFs helps to find the most optimal MOF for the intended application of researchers in each project.

Received 17th June 2025
Accepted 14th August 2025

DOI: 10.1039/d5ra04309c

rsc.li/rsc-advances

1. Introduction

Zirconium can be categorized as an infrequent element, making up around 0.023% of the Earth's crust.[1] This element is found in two forms: (1) white, suggesting its crystalline structure. (2) Blue-black powder form, suggesting that it is amorphous. Zirconium has many advantages over other transition metals, such as high mechanical and chemical stability of its products, spherical electron orbitals, low ionic radius, and electron pair acceptance capacity.[2–4] Zr ions are used as a metal to remove contaminants from the aqueous surroundings. Zr-based adsorbents are hard Lewis acids. They have properties such as high affinity for electronegative ligands, abundance in nature due to high production, low production cost, non-toxicity, environmental compatibility, low solubility in water, and inertness in redox and acid-based reactions.[1,5]

The growing interest in metal–organic frameworks (MOFs) stems from their structural versatility and the ability to tailor their chemical and physical properties by adjusting

School of Chemistry, College of Science, University of Tehran, Tehran, Iran, P.O. Box 14155-6455. E-mail: akhbari.k@ut.ac.ir; Fax: +98 21 66495291; Tel: +98 21 61113734

Pouya Khattami Kermanshahi

Pouya Khattami Kermanshahi is from Iran. He earned his MSc in Inorganic Chemistry from the University of Tehran in 2023. His research interests lie in the development of functional porous materials, particularly metal–organic frameworks (MOFs) and zeolitic imidazolate frameworks (ZIFs), with applications in antibacterial materials and environmental remediation. His work has focused on the design and characterization of MOF- and ZIF-based nanocomposites for antibacterial applications, drug delivery systems, and water purification. He has published several articles in the field of porous materials. Driven by a passion for sustainable technologies, he continues to explore materials that contribute to clean energy, pollutant removal, and advanced sensing platforms.

Pooria Refah

Pourya Refah graduated with a bachelor's degree in Chemistry from the University of Tehran in 2023. He is a chemist, and his research and studies focus on metal–organic frameworks (MOFs), including their structures, green and optimized synthesis methods for specific MOFs, as well as their applications in pharmaceuticals and drug delivery.

components such as metal nodes, organic linkers and overall topologies. Thus, manipulation of one of these parameters in their synthetic pathway will show completely different chemical and physical properties for them.[6,7] MOFs have opened up a fascinating new field of research into coordination compounds, with applications including catalysts,[8–10] electrochemical and chemical sensing[11–13] encapsulation of macromolecular compounds[14] and enzymes,[15,16] fuel cells,[17] gas storage,[18–20] removal of hazardous materials (such as heavy metals,[21,22] organic dyes,[23] greenhouse gases[24] and toxins[25]), water splitting,[26] anti-bacterial and bacteriostatic,[27–30] anti-cancer activities,[31–35] semi-conductors,[36] molecular reactors[37,38] chromatography,[39] drug delivery[40–42] and *etc.* The effectiveness of these metal frameworks is restricted in numerous critical applications due to the combination of two factors: the low stability of MOFs and the small sizes of their pores, especially when subjected to harsh conditions.[43] The primary condition to expand the efficiency of MOFs is to increase their chemical stability. According to Pearson's hard and soft acid and base principle (HSAB theory),[44] chemically stable MOFs can be obtained by using carboxylate ligands with low-capacity metal ions such as Zr^{4+}, Al^{3+}, Cr^{3+}, *etc* or produced low-capacity metal ions using azolate ligands such as Ni^{2+}, Zn^{2+}, Co^{2+}, *etc*.[45] As a case in point, Zr^{4+} carboxylate MOFs have improved research efforts since the discovery of **UiO-66**.[46] Despite the good stability of these MOFs compared to most reported MOFs, Zr-MOFs exhibit poor resistance against strong Lewis bases. Meanwhile, alkaline/nucleophilic conditions are prevalent in experimental applications, such as many catalytic coupling reactions.[43,47] The other group of stable MOFs comprises azolate ligands and low-transfer-capacity metal ions, which exhibit higher stability compared to their carboxylate counterparts under gaseous conditions.[48] Another method to enhance the stability of MOFs involves selecting nodes composed of relatively mild Lewis acidic species such as Zn^{2+} or Cu^{2+}. However, their weak coordination bonds make them susceptible to chemical attacks. To address this issue, clusters made of harder Lewis acid metals should be chosen as nodes. For instance, porphyrin Zr-MOFs demonstrate exceptionally high chemical stability.[49]

To overcome the limitations associated with small pore sizes and limited accessibility in many conventional MOFs, especially when dealing with large molecules or catalytic systems, the development of mesoporous structures has become increasingly important. According to IUPAC, mesoporous materials are defined as those possessing pore diameters between 2 and 50 nm, and various strategies have been developed to achieve this structure. Liu *et al.* classified these synthetic strategies into categories which can be listed like this. These strategies include incorporation of defects *via* ligand doping, the use of elongated organic linkers, stepwise assembly protocols, gelation, micro to meso conversion processes and topological control. Among these, topology directed design offers a unique route to introducing intrinsic microporosity without relying heavily on post-synthetic modifications or templating agents. This topological approach enables the creation of open, hierarchical and highly connected networks that maintain structural robustness while enhancing mass transport properties. Thus, understanding and controlling MOF topology is not only essential for improving stability, but also for rationally designing frameworks with mesoporous characteristics suited for advanced applications.[49] Guan and co-workers have elucidated reproducible and reliable methods to produce mesoporous and highly stable MOFs for future applications such as adsorption of large molecules, drug delivery, and size-selective catalysis. The reported methods include templating methods, with two subgroups: the single templating agent method and the cooperative template system; gelation process; methods that do not use templates; supercritical fluid synthesis, with two subgroups: CO_2-directed assembly method and ionic liquid/supercritical CO_2 emulsion technique; post-synthetic strategy, with two subgroups: hydrolytic post-synthetic methods and stepwise exchange of ligands; co-assembly of metal and ligand fragments; modulator-induced defect-formation strategy (which became very popular in recent years[50]) and encapsulation and etching method.[51] As a result, Albolkany *et al.* reported a new method for converting microporous materials to mesoporous ones through molecular surgery.[52] Creating clusters instead of simple metal ions was a turning point in the construction of MOFs. So far, zirconium-based clusters containing three to twelve metal atoms have been reported; however, in this context of MOFs, the most commonly observed nodes are Zr-based/oxo-cluster such as ZrO_6, ZrO_7 and Zr_6O_8. Notably, rare examples of larger cluster have been reported, including Zr_8O_6 in PCN-221 (ref. 53) and Zr_{12} clusters in CAU-45.[54] Among these, the Zr_6O_8 which often formulated as $[Zr_6(OH)_4(O)_6]$, is the most prevalent motif found in Zr-MOFs.[55,56] Zirconium-based MOFs represent a significant subclass that has garnered considerable attention since the first reported Zr-based MOF, UiO-66, where Zr_6 clusters and 12-connected inorganic linkers are connected.[46] Great efforts have

Kamran Akhbari

Kamran Akhbari joined University of Tehran, Department of Chemistry in 2013. He earned a Bachelor's Degree in Chemistry from Shahid Beheshti University in 2005, a Master of Science Degree in 2008 and PhD Degree in 2012 in Inorganic Chemistry from Tarbiat Modares University. He passed a post-doctoral fellow under the supervision of Prof. Ali Morsali at Tarbiat Modares University. He has published more than 150 papers and his current research focuses on the crystal engineering of coordination polymers and supramolecular compounds, metal–organic frameworks (MOFs) and their potential applications in energy storage materials, separation, drug delivery and catalysis. He also researches in synthesis and characterization of nano-scale materials. In 2013, he won the second place in the Khwarizmi Young Award for his work in the field of modulating methane storage in nanoporous anionic MOFs via post synthetic cation exchange process.

been dedicated to developing this subclass of MOFs based on edge-transitive nets, owing to the increasing interest in reticular chemistry and the versatility of Zr-cluster connectivity.[55] Therefore, due to the unique properties of Zr-based MOFs and their widespread applications as adsorbents, it is necessary to develop their behavioral and functional properties for further exploration. According to Scopus (Fig. 1), there has been a growing trend in technical work on MOFs over the past decades, with each year witnessing a greater percentage of studies conducted on their zirconium-based subgroup. Zr-based materials show a great range of applications in drug delivery and water treatment. Although there are only a few review articles on zirconium, they all focus on the investigation of Zr-MOFs.[57–60]

Moreover, Zr-based MOFs have served as templates to achieve mesoporous materials in many studies, such as K-ZrO_2, which was designed using the **UiO-66** template, as reported by Wang *et al.*[61] or synthesis of yttria-stabilized zirconia (YSZ) with the same template reported by Yue *et al.*[62] A comprehensive review on the conversion of MOFs and coordination polymers into functional materials with nanostructures, such as metal oxides, carbon nanoparticles, porous carbons, and composites, has been published by Lee *et al.* They place particular emphasis on understanding the connection between the nature of the parent frameworks and the resulting nanomaterials. They discuss various experimental approaches based on mechanistic perception.[63]

In this study, 10 topologies that appear in published mesoporous Zr-based MOFs will be investigated, and we will discuss their special properties. The applications of these structures are strongly influenced by their topologies, and the authors have concluded that knowing the topology and, more generally, the

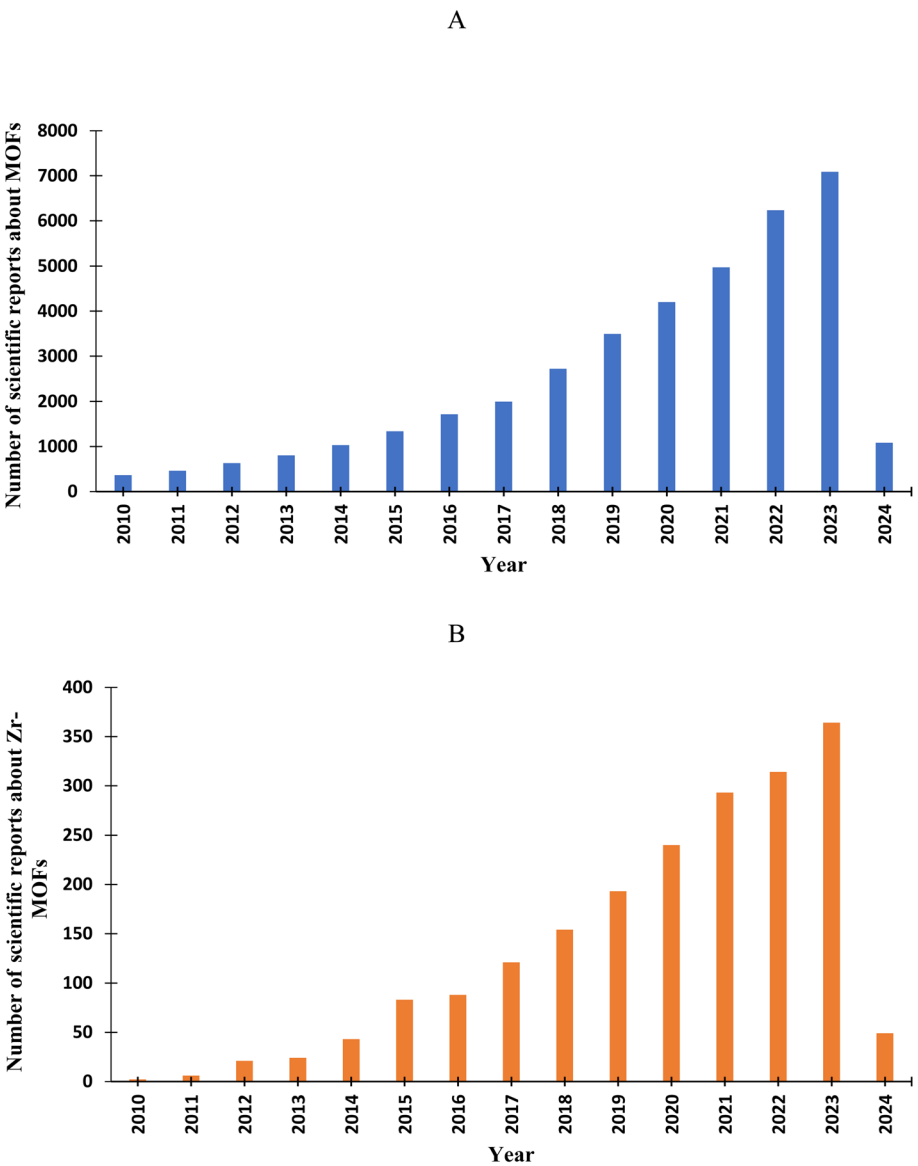

Fig. 1 Bibliometric analysis database of Scopus, showing published articles between 2010 to 2024. (A) About MOFs and (B) about Zr-based MOFs.

Table 1 Overview of Zr-based MOFs discussed in this review, including their structural features, topologies, and key properties[d]

	MOF	Linker	Cluster/core	Surface area ($m^2\ g^{-1}$)	Topology	Thermal stability (°C)	Pore size (Å)	Ref.
1	BUT-12	$CTTA^{3-}$	$Zr_6O_4(OH)_8(H_2O)_4$	3387	the, (3,8 connected)	320	13 and 21	77
2	BUT-13	$TTNA^{3-}$	$Zr_6O_4(OH)_8(H_2O)_4$	3948	the, (3,8 connected)	430	14 and 28	77
3	CAU-45	5-Acetamidoisophthalic acid	$Zr_6(\mu_3\text{-}O)_4(\mu_3\text{-}OH)_4$, $Zr_{12}(\mu_3\text{-}O)_8(\mu_3\text{-}OH)_8(\mu\text{-}OH)_6]^b$	NR[a]	NR[a]	330	17–22	54
4	Ce/Zr-DUT-67-pzd	TDC^-	$[Zr_6O_6(OH)_2(tdc)_4(CH_3COO)_2]$	781.8	reo, (8,4 connected)	350	10	78 and 79
5	Ce/Zr-MOF-808	BTC^{3-}	$Zr_6(\mu_3\text{-}O)_4(\mu_3\text{-}OH)_4$	2060	spn, (3,6 connected)	550	7–10	79 and 80
6	Ce/Zr-UiO-66	BDC^{2-}	$[Zr_6(\mu_3\text{-}O)_4(\mu_3\text{-}OH)_4]$	1187	fcu, (12-connected)	450–600	6	79 and 81
7	*c*-(4,12)MTBC-M6	MTBC	$Zr_6O_4(OH)_4$	NR[a]	(4,12) connected	NR[a]	NR[a]	82
8	DUT-126	TDC^{2-}	$Zr_6O_4(OH)_4$	1297	hbr, (8,8-connected)	250	22.8, 11.8, 5.3	75
9	Meso UiO-66-$(OH)_2$	BDC-$(OH)_2{}^{2-}$	$Zr_6(\mu_3\text{-}O)_4(\mu_3\text{-}OH)_4)$	940	fcu, (12-connected)	300–500	26	83
10	Meso UiO-66-NH_2	BDC-$NH_2{}^{2-}$	$Zr_6(\mu_3\text{-}O)_4(\mu_3\text{-}OH)_4)$	1410	fcu, (12-connected)	300–500	28	83
11	MIP-206	IPA^{2-}	$Zr_6(\mu_3\text{-}O)_4(\mu_3\text{-}OH)_4$, $Zr_{12}(\mu_3\text{-}O)_8(\mu_3\text{-}OH)_8(\mu\text{-}OH)_6]^b$	NR[a]	NR[a]	450	25–27°	84
12	MOF-545	$MTCPP^{4-}$	$Zr_6(\mu_3\text{-}OH)_8$	2220	csq, (4,8 connected)	300	13, 37	85
13	MMU	BDC^{2-}	NR[a]	453.8	NR[a]	NR[a]	35–70	86
14	MOF-526	TCBPP	$[Zr_6(OH)_4O_4(CO_2)_{12}]$	4260	ftw, (4,12 connected)	400	25.5	87
15	MOF-527	TCTPP	$[Zr_6(OH)_4O_4(CO_2)_{12}]$	2000	ftw, (4,12 connected)	400	31.4	87
16	MOF-528	TCTTPP	$[Zr_6(OH)_4O_4(CO_2)_{12}]$	3550	ftw, (4,12 connected)	400	37.6	87
17	MOF-808	BTC^{3-}	$Zr_6(\mu_3\text{-}O)_4(\mu_3\text{-}OH)_4$	2060	spn, (3,6 connected)	550	7–10, 18.4	80
18	NU-1000	$TBAPy^{4-}$	$Zr_6(\mu_3\text{-}OH)_8$	2320	csq, (4,8-connected)	500	14, 30	88
19	NU-1003	$TNAPy^{4-}$	$Zr_6(\mu_3\text{-}OH)_8$	2700	csq, (4,8-connected)	NR[a]	38–45	89
20	NU-1008	TCPB-$Br_2{}^{4-}$	$Zr_6(\mu_3\text{-}O)_4(\mu_3\text{-}OH)_4(HCOO)_4(OH)_{3.5}(H_2O)_{3.5}$	NR[a]	csq, (4,8-connected)	NR[a]	13, 30	90
21	NU-1010	$TPCB^{4-}$	$Zr_6(\mu_3\text{-}OH)_8$	2040	csq, (4,8-connected)	500	NR[a]	91
22	NU-1105	PY-FP^{4-}	$Zr_6(\mu_3\text{-}O)_4(\mu_3\text{-}OH)_4$	5645	ftw, (4,12-connected)	470	NR[a]	92
23	NU-1200	$TMTB^{4-}$	$Zr_6(\mu_3\text{-}OH)_8(OH)_8$	2400	the, (3,8-connected)	300	14, 20	66
24	NU-1601	PET-2^{6-}	$Zr_6(\mu_3\text{-}O)2(\mu_3\text{-}OH)6(HCOO)(OH)(H_2O)$	3970	alb, (6,12-connected)	500	14, 22	74
25	NU-1602	PET-3^{6-}	$Zr_6(\mu_3\text{-}O)2(\mu_3\text{-}OH)6(HCOO)(OH)(H_2O)$	4500	alb, (6,12-connected)	480	17, 27	74
26	NU-500	TCPB-$Br_2{}^{4-}$	$Zr_6(\mu_3\text{-}O)_4(\mu_3\text{-}OH)_4(HCOO)_4(OH)_{3.5}(H_2O)_{3.5}$	NR[a]	(4,4,4,5-Connected net[b]	NR[a]	9 × 10	6
27	NU-901	$TBAPy^{4-}$	$Zr_6(\mu_3\text{-}OH)_8$	1365	scu, (4,8-connected)	NR[a]	12	93
28	NU-906	TCPB-$Br_2{}^{4-}$	$Zr_6(\mu_3\text{-}O)_4(\mu_3\text{-}OH)_4(HCOO)_4(OH)_{3.5}(H_2O)_{3.5}$	NR[a]	scu, (4,8-connected)	NR[a]	12 × 27	6
29	NU-600	TCPB-$Br_2{}^{4-}$	$Zr_6(\mu_3\text{-}O)_4(\mu_3\text{-}OH)_4(HCOO)_4(OH)_{3.5}(H_2O)_{3.5}$	NR[a]	she,(4,6-connected)	NR	13 × 19	6
30	NUPF-1	[c]	$Zr_6(\mu_3\text{-}O)_4(\mu_3\text{-}OH)_4$	NR[a]	scu, (4,8-connected)	450	23–51	94
31	PCN-128	$ETTC^{4-}$	$Zr_6(\mu_3\text{-}OH)_8$	2000	csq, (4,8-connected)	400	38/35, 15	89

Table 1 (*Contd.*)

	MOF	Linker	Cluster/core	Surface area ($m^2\ g^{-1}$)	Topology	Thermal stability (°C)	Pore size (Å)	Ref.
32	PCN-221	$TCPP^{4-}$	$Zr_6(\mu_4\text{-}OH)_8$	1936	6,4-Connected	450	11, 20	53
33	PCN-608	$TPCB^{4-}$	$Zr_6O_4(OH)_8(H_2O)_4$	~800	csq, (4,8-connected)	300	33	91
34	PCN-808	$TPTB^{4-}$	$Zr_6(\mu_3\text{-}O)_4(\mu_3\text{-}OH)_4$	2380	csq, (4,8) connected	NR[a]	12, 25–31	95
35	Tr-(4,12)MTBC-M6	MTBC	$Zr_6O_4(OH)_4$	NR[a]	(4,12) connected	NR[a]	NR[a]	82
36	UiO-66	BDC^{2-}	$Zr_6(\mu_3\text{-}O)_4(\mu_3\text{-}OH)_4$	1187	fcu, (12-connected)	450–600	6	46
37	UPC-612	H_4L-L	$Zr_6O_4(OH)_4$	2016	ftw, (4,12-connected)	NR[a]	14, 20	96
38	UPC-613	H_4L-s	$Zr_6O_4(OH)_4$	853	ftw, (4,12-connected)	NR[a]	7, 12	96
39	WM-MOF	Ni-tcpp	$Zr_6(\mu_3\text{-}OH)_8$	1724	csq, (4,8-connected)	350	22.8	97
40	Zr-TTFTB	$TTFTB^{4-}$	$Zr_6O_8(OH_2)_8$	1353	scu, (4,8-connected)	400	13.7	98
41	Zr-MeTTFTB	Me-$TTFTB^{4-}$	$[Zr_6O_4(OH)_4(PhCOO)_6(COO)_6]$	1932	she, (4,6-connected)	400	12.6, 15.8, 20.7	98

[a] NR: not reported. [b] New topology which were not named. [c] A porphyrin carboxylate ligand. [d] H_3CTTA: 5′-(4-carboxyphenyl)-2′,4′,6′-trimethyl-[1,1′:3′,1″-terphenyl]-4,4″-dicarboxylic acid). H_3TTNA = 6,6′,6″-(2,4,6-trimethylbenzene-1,3,5-triyl)tris(2-naphthoic acid). H_2TDC: thiophene-2,5-dicarboxylate. H_3BTC benzene 1,3,5-tricarboxylate. H_2BDC: benzene-1,4-dicarboxylate. IPA: isophthalic acid. MTCPP: [5,10,15,20-tetrakis(4-carboxyphenyl)porphyrinato]-M (MTCPP (M = Mn(III), Fe(III) and Cu(II)) H_4TBAPy: 1,3,6,8-tetrakis(*p*-benzoic acid)pyrene. H_4TNAPy: 1,3,6,8-tetra(6-carboxynaphthalen-2-yl)pyrene. TCPB-Br_2: 1,4-dibromo-2,3,5,6-tetrakis(4-carboxyphenyl)benzene. TPCB: 3,3′,5,5′-tetrakis(4-carboxyphenyl)-1,1′-bipheny. TMTB: 4,4′,4″-(2,4,6-trimethylbenzene-1,3,5-triyl)tribenzoic acid. H_4ETTC: 4,4′,4″,4‴-(ethene-1,1,2,2-tetrayl)tetrakis (([1,1′-biphenyl]-4-carboxylic acid)). H_4TPTB = 5′,5‴-bis(4-carboxylatophenyl)-4‴,6′-dimethoxy-[1,1′:3′,1″:4″,1‴:3‴,1⁗-quinquephenyl]-4,4⁗-dicarboxylate. Ni-TCPP: nickle-tetrakis(4-carboxyphenyl)-porphyrin. BDM: benzene1,3-dimesitylenic acid.

structure of MOFs helps to find the most optimal MOF for the intended application in each research project.

2. Discussion

2.1 Structure and topology

David Brown defined topology as the three-dimensional spatial arrangement of atoms in materials. The structural variety and topology of MOFs arise from various ways in which ligands and clusters connect. Topology in MOFs is influenced by ligands and their spatial orientation, clusters and their connectivity, and environmental conditions.[64] In many studies, researchers are trying to maintain the topology intact during ligand enlargement or reduction of connectivity by using modulators, which has shown the importance of topology.[65]

Topologies of Zr-based MOF include these topologies but as we know all topologies are not limited to these items:

csq (*e.g.*, **NU-1000** and **PCN-222**/**MOF-545** (ref. 45 and 66)), **scu** (*e.g.*, **nu-902** (ref. 67)), **spn** (*e.g.*, **MOF-808** (ref. 68)), **the** (*e.g.*, NU-1200 (ref. 69)/**BUT-12** (ref. 70)), **she** (*e.g.*, **nu-600** (ref. 71)), **ftw** (*e.g.*, **MOF-1211** (ref. 72)), **reo** (*e.g.*, **DUT-51** (ref. 73)), **flu** (*e.g.*, **PCN-521** (ref. 74)), **hbr** (*e.g.*, **DUT-126** (ref. 75)) and **alb** (*e.g.*, **NU-1601** (ref. 76)) Table 1 shows that complete list of these topologies.

This review will focus on studies which are done from 2015 until 2021 that whose main research topics were mesoporous Zr-based MOFs.

Illuminating the dominating parameters of MOFs, such as topology, thermal and chemical stability, and porosity, is not simple. Since the first Zr and tetra-topic linker MOFs, numerous topologies have been reported, which can be attributed to the linker conformation and connectivity of clusters. These are influenced by various synthetic conditions such as modulating reagent and its concentration, metal salt as a precursor, temperature, solvent, and reagent concentration.[45,49] The topologies of reported Zr-MOFs and their applications dependent on structure are discussed in the following sections.

2.2 csq topology

The **csq** topology is one of the most famous and frequently reported topologies among Zr-based MOFs. This topology provides two kinds of channels with different shapes and sizes, referred to as the hierarchical model; one central hexagonal channel is surrounded by six triangular channels.[99]

This topology was observed in **NU-1000**, first reported by Mondloch *et al.* They studied the post-synthesis metalation from the vapor phase (AIM) on **NU-1000**. When choosing a suitable MOF for the AIM process, three design criteria should be considered: 1. meso channels, 2. thermal and hydrolytic stability, and 3. spatially oriented functional groups. **NU-1000**, with 30 Å meso channels and the **csq** topology, a 4,8-connected topology with 8-connected $Zr_6(\mu_3\text{-}OH)_8$ clusters and 4-connected 1,3,6,8-tetrakis(p-benzoic acid)Pyreme linkers (see Fig. 2), maintains stability up to 500 °C, fulfilling all three criteria. This MOF provides the best template for demonstrating quantitative and self-limiting metalation by AIM. It consists of eight nodes,

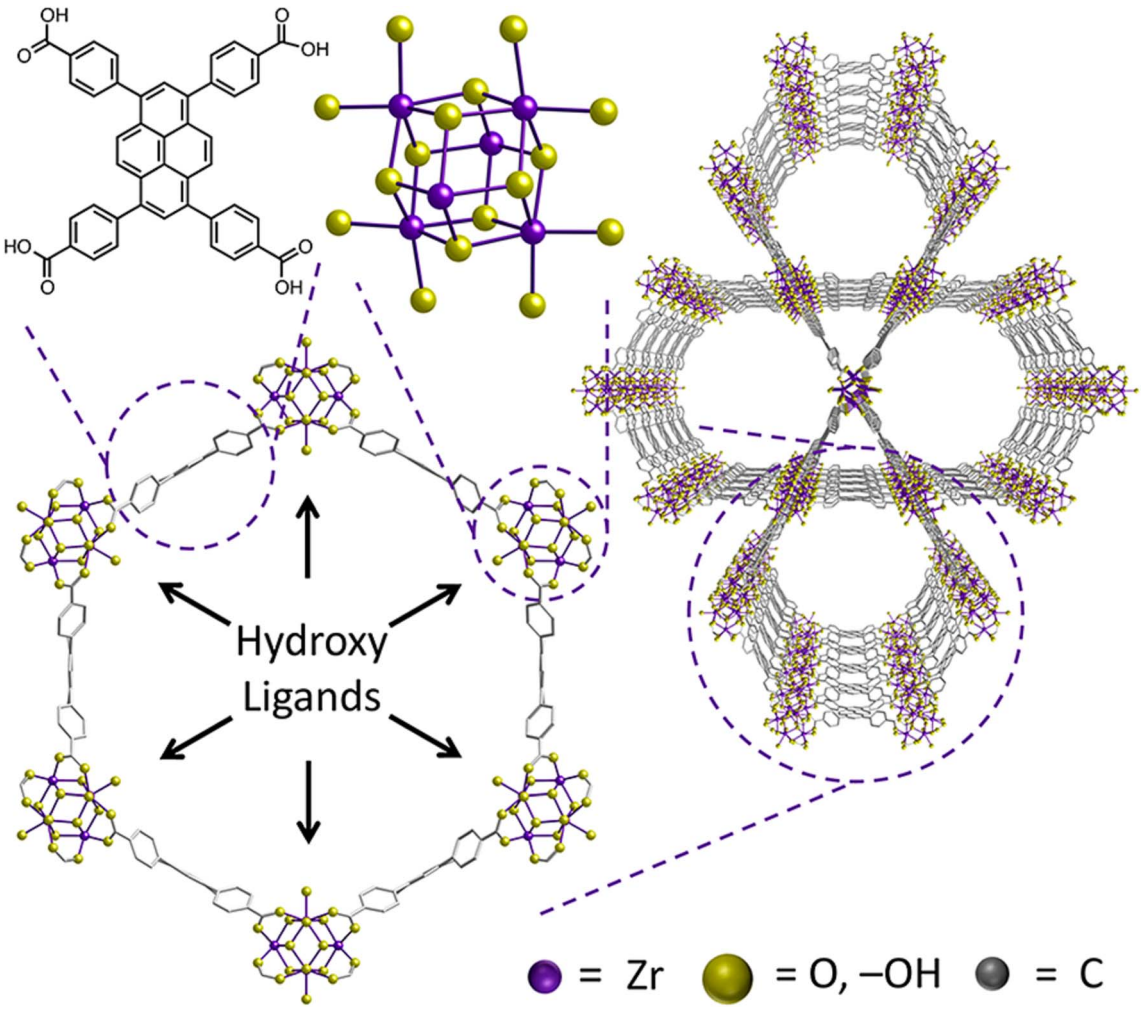

Fig. 2 Schematic of **NU-1000**, without hydrogen atoms which are hidden for better understanding.[88] From ref. 88 with permission. Copyright 2013, American Chemical Society.

each comprised of a Zr_6 cluster in the shape of an octahedron, topped by eight μ_3-OH ligands.[88]

Pankajakshan *et al.* described **NU-1000** as including 8-connected $Zr_6(\mu_3\text{-}O)_4(\mu_3\text{-}OH)_4(H_2O)_4(OH)_4$ nodes interconnected with 1,3,6,8-(*p*-benzoate)-pyrene, also known as $TBAPy^{4-}$ linkers. In contrast, **UiO-67** contains 12-connected $Zr_6O_4(OH)_4$ cluster nodes and linear 4,4′-biphenyl dicarboxylic acid (BPDC) ligands, and both materials are water-stable. **NU-1000** exhibits a face-centered cubic organization of clusters with six Zr atoms and features both free and bridging –OH and H_2O groups. Additionally, **NU-1000** has wide mesoporous channels (31 Å), while **UiO-67** possesses two cages in the form of octahedral (16 Å) and tetrahedral (14 Å). Both materials are recognized as hierarchical structures[100] (in the next section, UiO-67's topology will be discussed).

These MOFs were employed for the removal of toxic glyphosate molecules from wastewater. It was demonstrated that the adsorption efficiency increases with the reduction in MOF size. In **NU-1000**, this effect was pronouncedly better compared to **UiO-67**. The relationship between MOF samples and glyphosate was observed in all experiments. It was found that all the samples maintained their structural morphology after glyphosate adsorption. An increase in the amount of phosphorus resulted in a reduction in particle sizes. The stability of washed samples was assessed using powder XRD, which revealed that the structure of **NU-1000** remained stable even after washing. However, **UiO-67** samples were lost after washing, highlighting the advantage of **NU-1000** and its **csq**-net topology over **UiO-67**.

Topology not only influences applications but also can affect post-synthetic modifications. Choi *et al.* demonstrated a post-synthetic modification (PSM) that involved adding iron thiolate to **NU-1000**. They used this catalyst to convert NO^{3-} to NH^{4+}. Although this group studied the catalytic performance of the new material using the Brunauer–Emmett–Teller (BET) theory analysis, which revealed a reduction in surface area from 2260 $m^2\ g^{-1}$ to 320 $m^2\ g^{-1}$, showing that the 1.2 nm triangular channel had completely disappeared and the meso channels remained unoccupied due to the presence of the FeSC12-AIM substrate inside the channels (Fig. 3).[8]

Nu-1000 was used as a propane oxidizer at a low temperature by Li *et al.* They have used **NU-1000** as a supporter for heterogenic Co^{2+} catalyst that reduces reaction temperature from 300–

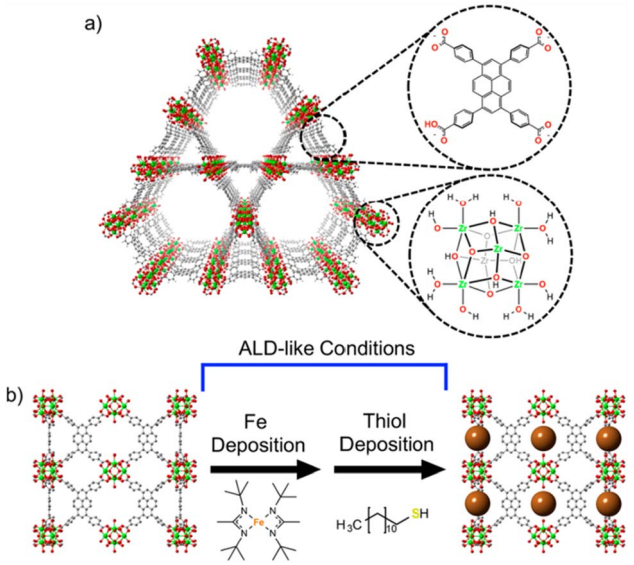

Fig. 3 (a) Structure of the NU-1000 and its 6 metal cluster and pyrene-based linker that includes the binding sites for iron thiolate precipitation and deposition, which are zoomed in (b) the ALD procedure of iron thiol cluster generation in the MOF.[8] From ref. 9 with permission. Copyright 2019, American Chemical Society.

350 °C (in case of VO_x to 200 °C). Their crystalline structure gives the opportunity to perform mechanism studies accurately. On its Zr_6 nodes, Co^{2+} is present as a catalyst. Cobalt is located in MOF structure with two methods of SIM and AIM. The structure of **NU-1000** has a central hexagonal channel surrounded by hexagonal channels, and the product is called **Co-SIM-NU-1000** and **Co-AIM-NU-1000**. These two products have oxidized propane to propene at 230 °C in the presence of the oxygen. They obtained that the best result occurs while using **Co-SIM-NU-1000**. The metalation process is associated with adding cobalt to the inside, which does not disrupt the structure. Ligand is pyrene based, and its long nature helps to stop the sintering process and keeps the surface area wide. The behaviors of **Co-SIM-NU-1000** and **Co-AIM-NU-1000** are different. When activated with oxygen, a new Co–Co bond is formed in Co-AIM that is not in Co-SIM. This reduces the surface of cobalt catalysts to be available in AIM.[101]

Li *et al.* synthesized a framework illustrating a pore size near 3.8–4.5 nm and the **ftw** topology to encapsulate and immobilize a nerve agent named OPAA. Unlike previous studies using micropore immobilizers, **NU-1000** was utilized in this study, resulting in higher enzymatic activity compared to previous methods. Previous attempts to increase the pore size of **NU-1000** by introducing single or triple C–C bonds in the connecting structure failed, leading to the creation of an isomorph MOF with the **ftw** topology each time. To address this issue, Li *et al.* utilized a tetra-carboxylate pyrene-based linker and DMF as a solvent, with trifluoroacetic acid as a modulator, to produce **NU-1003** with the same **csq** topology as **NU-1000**. They reported two different pore sizes: 4.4 nm hexagonal and 1.7 nm triangular pores, as expected in the **csq**-net, which were slightly larger than the previous attempts by this team. Additionally, Li *et al.* used **PCN-128** with **csq** topology and 4.2 nm hexagonal pores and 4 nm triangular pores. This MOF was first reported and characterized by Zhang *et al.*[74] In both of Li's studies, OPAA was immobilized, and its enzymatic activity was measured. The **csq** topology proved to be particularly suitable for this study due to the hierarchical structure with a wide window between meso and micro cavities, allowing the enzyme to be in proximity to infiltrated reactants. The **NU-1003** and **PCN-128** windows

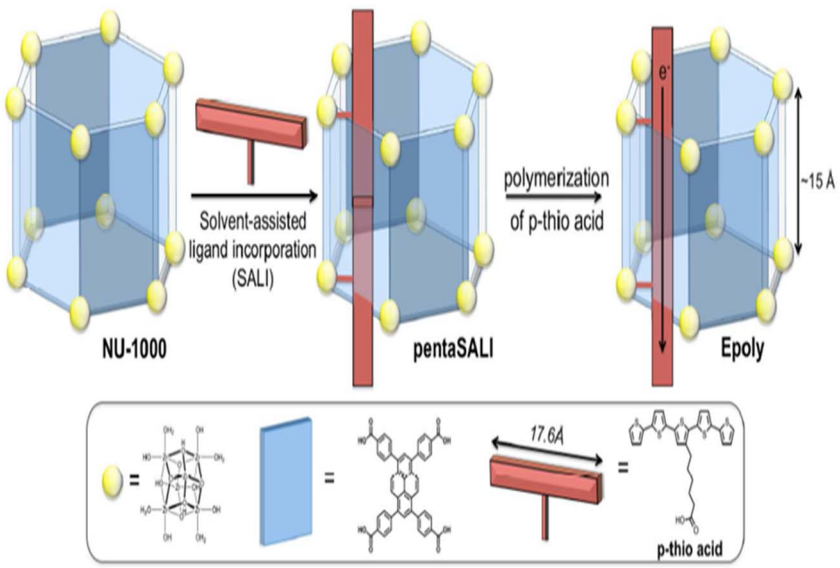

Fig. 4 Schematic illustration of the solvent-assisted ligand incorporation (SALI) process used to modify NU-1000 with a pentathiophene-based conductive polymer. The deprotonated *p*-thio acid molecules are selectively grafted onto the Zr_6 nodes, forming conductive polymer strands within the larger channels of the hierarchical MOF structure. This post-synthetic modification preserves the framework's porosity and high surface area while enabling electrical conductivity. The schematic is conceptual and does not imply strict alignment of the polymer strands along the channel direction or their exclusive orientation.[108] From ref. 108 with permission. Copyright 2017, American Chemical Society.

measured 12 × 13 Å and 9 × 9 Å, respectively. To determine the capacity of OPAA to load into **NU-1003**, crystals of different sizes were placed in BTP (bis-tris-propane) buffer with a pH 7.2 solution of OPAA. After OPAA immobilization, the volume of triangular channels decreased from 0.20 to 0.15 $cm^3\ g^{-1}$, and hexagonal channels decreased from 0.45 to 0.14 $cm^3\ g^{-1}$ in OPAA@**NU-1003**-size compared to **NU-1003**-size. This indicated that OPAA had filled the hexagonal channels while the micropores were relatively unoccupied. The study then investigated the enzyme activity after OPAA immobilization and the effect of particle size on the hydrolysis of DFP (as a nerve agent simulation) and Samon (an actual nerve agent). The catalytic performance of the immobilized OPAA in the mesoporous MOF was improved compared to free OPAA in the BTP buffer.[65,102]

Noh *et al.* reported the use of **NU-1000** to immobilize molybdenum oxide as a cyclohexane oxidation catalyst. The resulting Mo-SIM is comparable to Mo-ZrO_2 but avoids the inefficiency associated with the formation of Mo-ZrO_2. **NU-1000** was chosen due to its excellent crystal structure, distinct topology, and thermal stability. The hierarchical structure with pores ranging from 10 to 31 Å facilitates optimal diffusion and accessibility of active sites.[103]

As mentioned above, the **csq** topology with fully available metal nodes is one of the best candidates for the AIM process. Rimoldi *et al.* have introduced a new atomic layer deposition method using $[AlMe_2(oipr)]_2$ instead of the classic $[AlMe_3]$ to deposit aluminum onto Zr clusters. This new material, **Al-NU-1000**, exhibits high thermal stability, with aluminum replacing hydrogen in terminal ligands such as OH- and H_2O. The superiority of $[AlMe_2(oipr)]_2$, also known as "DAMI," lies in its ability to maintain a tetrahedral spatial configuration in the vapor phase, enabling its use in gas-phase electron diffraction. However, the use of DAMI results in self-limitation of the reaction and a reduction in the reaction rate, leaving some coordination sites unoccupied. The ratio of Al/Zr_6 is reported as 7.[104]

Chen *et al.* used MOFs as absorption cooling systems based on the absorption and desorption of propane and isobutane. They used two frameworks with **csq** topology, 8-connected Zr_6O_8 cluster, and tetra topic linkers (**NU-1003** $TNAPy^{4-}$ and **NU-1000** $TBAPy^{4-}$) display two kinds of pores: micro triangular channels and meso hexagonal channels. Its obvious larger ligand in **NU-1003** results more extensive channels (4.7 nm for central hexagonal channel's diameter in **NU-1003** towards 3.3 nm in **NU-1000**). They have shown the mechanism of absorption flows in two steps (type IV), in which micro channels are filled the same as meso channels consecutively. Also, they have established the relationship between absorber dimensions and cooling capacity when wider channels for **NU-1003**, saturation loadings of both absorbent components are significantly larger than in **NU-1000**, in their past studies using **MIL-101** as an absorbing agent showed weaker performance because of the lower saturation loading (in **NU-1000** is 1 g/1 g, in **NU-1003** is 1.4 g/1 g and in **MIL-101** is 0.5 g/1 g). They used these MOFs for refrigeration, ice-making, and also heat pumps because these applications were very common with raising adsorption pressures. According to Lange *et al.* cooling capacity is described as the latent heat of the refrigerant at the working capacity multiplied by the evaporator temperature, which is the maximum amount of cooling compounds that can be desorbed from the MOFs surface upon heating.[105] The working capacity could depend on the difference in the refrigerant uptake, like temperature and pressure.[106]

Wang *et al.* studied the unsaturated clusters in **NU-1000** and its performance in PSM, attributing its effectiveness to its topology. Despite the wide range of applications of MOFs, progress has reached a bottleneck in areas such as fuel cells and supercapacitors, which require low energy charge transfer. Various methods have been explored to increase MOF conductivity, but they often result in a reduction of the BET surface area to less than 1000 $m^2\ g^{-1}$ or a change in topology, leading to the formation of amorphous products. For example, Talian *et al.* proposed bridging the metal nodes with new guest molecules to create a suitable path for conducting electric charge.[107] The method used in this study involved solvent-assisted ligand incorporation (SALI), employing a pentathiophene molecule, which is the deprotonated form of *p*-thio acid. This molecule features a carboxylate group on a flexible carbon chain, allowing it to be grafted onto the nodes of **NU-1000** in a self-limiting manner. This process only reduces the pore size from 31 Å to 27 Å, leaving approximately 73% of the MOF's space unoccupied. The resulting BET surface area is 1600 $m^2\ g^{-1}$, significantly higher than that of porous carbon. The conductivity of

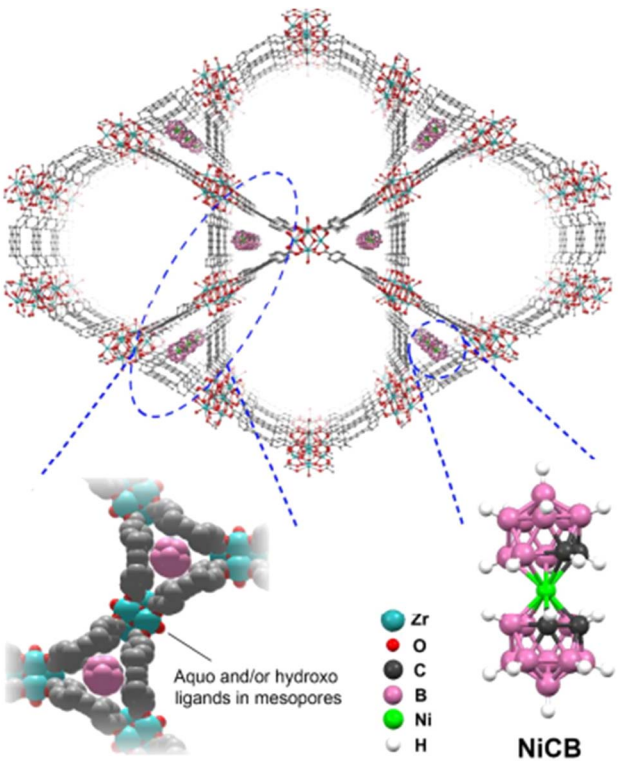

Fig. 5 The crystalline structure of NiCB@NU-1000 with occupied triangular channels and lack of hydrogen atoms. Triangular shaped channels of NiCB@NU-1000 are also demonstrated in below to illustrated the close interaction between NiCB and three neighbor pyrenes. Also there is presentation of NiCB.[109] From ref. 109 with permission. Copyright 2018, American Chemical Society.

the material varies depending on the thiophene doping level, ranging from 0 to 1.7×10^{-7} s cm^{-1}. Strands of the conductive polymer formed post-synthetically on the inner surface of the wide channels of **NU-1000** are selectively positioned in the larger channels. The hierarchical nature of **NU-1000** provides both vacant channels and intact porosity, facilitating this process.[108] Fig. 4 shows the performance of modified MOF after *p*-thio acid addition.

High stability against water in a broad-ranging of pH values of zirconium-based MOFs is reputed, which is the reason why these MOFs are suitable to use in aqueous conditions like hydrogen progress catalysis and adsorption of water from air. Kung *et al.* tried to increase the electrical conductivity of MOFs by using metallacarboranes. In this way, they introduced **NiCB@NU-1000** and showed the potential of using these conductive metallacarboranes in electrochemical uses. To examine its redox activity, **Mn-AIM-NiCB@NU-1000** was produced after manganese oxide was presented in **NiCB@NU-1000**. It can be seen in Fig. 5 that, NiCB existed in all the triangular shaped channels of **NU-1000** at 100% occupancy. ICP-OES measurements of **NiCB@NU-1000** samples in digested form showed a loading of 0.74 ± 0.07 NiCB per each node.[109]

Kung *et al.* also studied the rendering of mesoporous electroconductive MOFs and their chemical responsiveness. They utilized **NU-1000** and rendered it electronically conductive through a robust inorganic approach that preserved the material's structure and porosity. This approach relies on the condensed-phase bonding of tin species molecules onto MOF

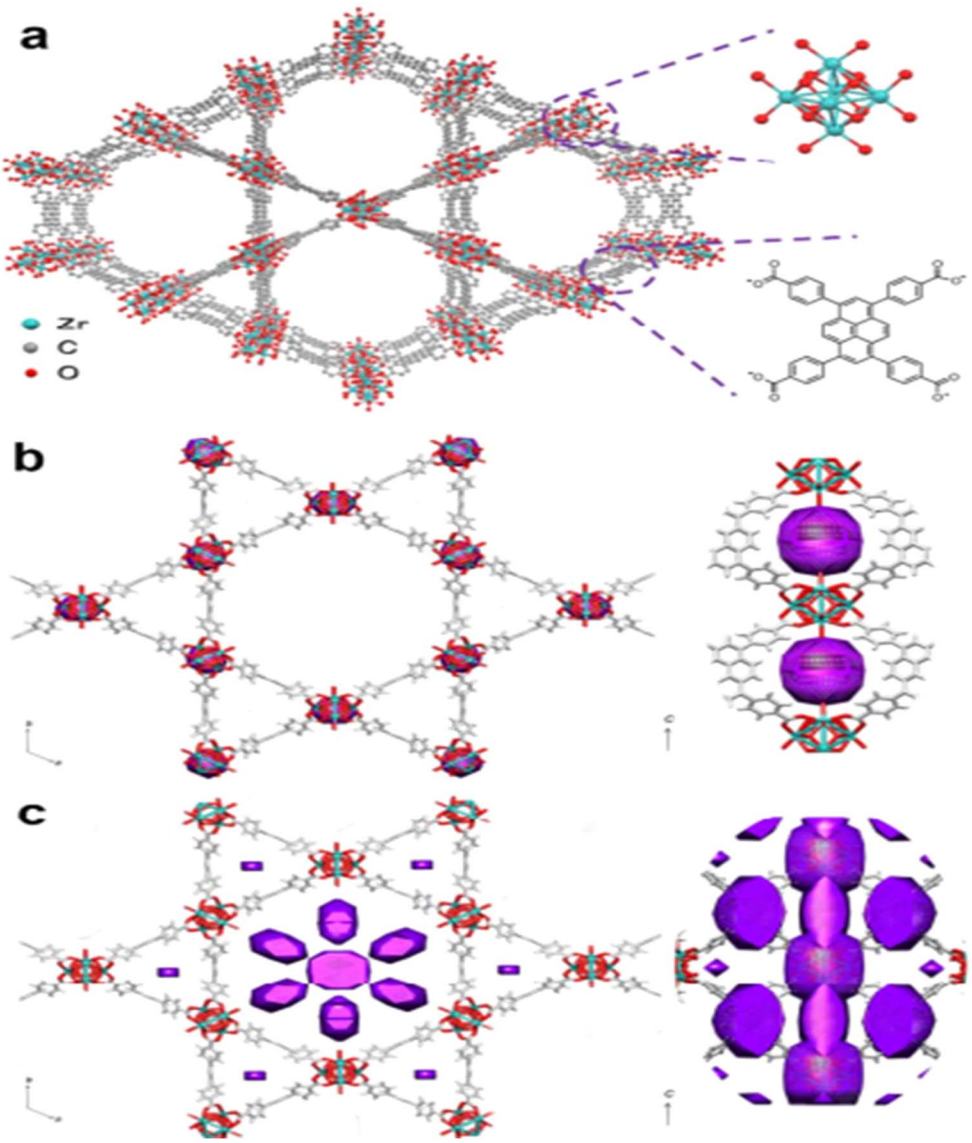

Fig. 6 Schematic representation of **NU-1000** and the progression of the single-ion metathesis (SIM) process used to incorporate tin oxide into the framework. (a) Top-view of the **NU-1000** crystal structure (hydrogen atoms omitted for clarity). (b) Electron density difference (EDD) map after one SIM cycle, showing initial incorporation of Sn(IV) species. (c) EDD map after three SIM cycles, indicating increased tin loading. The purple regions represent the electron density associated with tin oxide clusters bonded to the Zr_6 nodes. This post-synthetic modification preserves the mesoporous framework of **NU-1000** while introducing electroconductivity *via* irreversible bonding between Sn species and node-bound hydroxyl and aqua ligands.[110] From ref. 110 with permission. Copyright 2018, American Chemical Society.

clusters. Specifically, this single-ion metathesis (SIM) method is employed to connect tin oxide clusters uniformly across 1D hexagonal and triangular meso- and microporous channels *via* irreversible reactions with hydroxyl and aqua ligands. These ligands are presented at the surface of the node with a ratio of 4.3, 9, and 14 tin(IV) ions per Zr6 cluster after one, two, and three cycles of SIM, respectively.[110] In this case before the increment of the metal index and also after that, this process can be compared with Fig. 6.

The target of Li and Gao *et al.* study was confined nano BiOI particles into **NU-1000** with **csq** topology with two steps: first, be in the vicinity with $Bi(NO_3)_3 \cdot 5H_2O$ to produce **Bi^{3+}@NU-1000** then, reacts with KI in ethylene glycol/H_2O results in **BiOI@NU-1000** used for valid photocatalytic hydrogen development in the presence of visible light.

Hierarchical structure, with pore widths of 31 and 10 Å, which makes **NU-1000** a highly porous structure, high water, and weak acids stability, which was discussed in the first section, homogeneous distribution of Brønsted acids, –OH/–OH_2 groups, at the Zr_6 clusters, which facilitated metalation and based on McGonigal and Deria *et al.* **NU-1000** acts as a redox-type photosensitizer and n-type semiconductor,[92,111] all are reasons that according to that, Li *et al.* chose **NU-1000** to merge the BiOI particle.[112]

The main focus of Kato *et al.*'s study revolves around the removal of pollutants and heavy metals utilizing Zr-based MOFs. They investigated the energetics of interactions between MOFs, specifically the well-known **csq** topology MOFs **NU-1000**, **NU-1010**, and **PCN-608-OH**, and toxic species. Within the **csq** topology, there are two unoccupied spaces for chemical absorption: smaller triangular channels and larger hexagonal channels. Their investigation considered both enthalpic and entropic parameters, revealing **NU-1000**'s favorable enthalpic and entropic characteristics for absorption. In the absorption process of uremic toxins in mesopores, the primary driving force is entropic, while in other sites within smaller pores, referred to as cite one and cite two, absorption is driven by both enthalpic and entropic factors. Specifically, the adsorption of

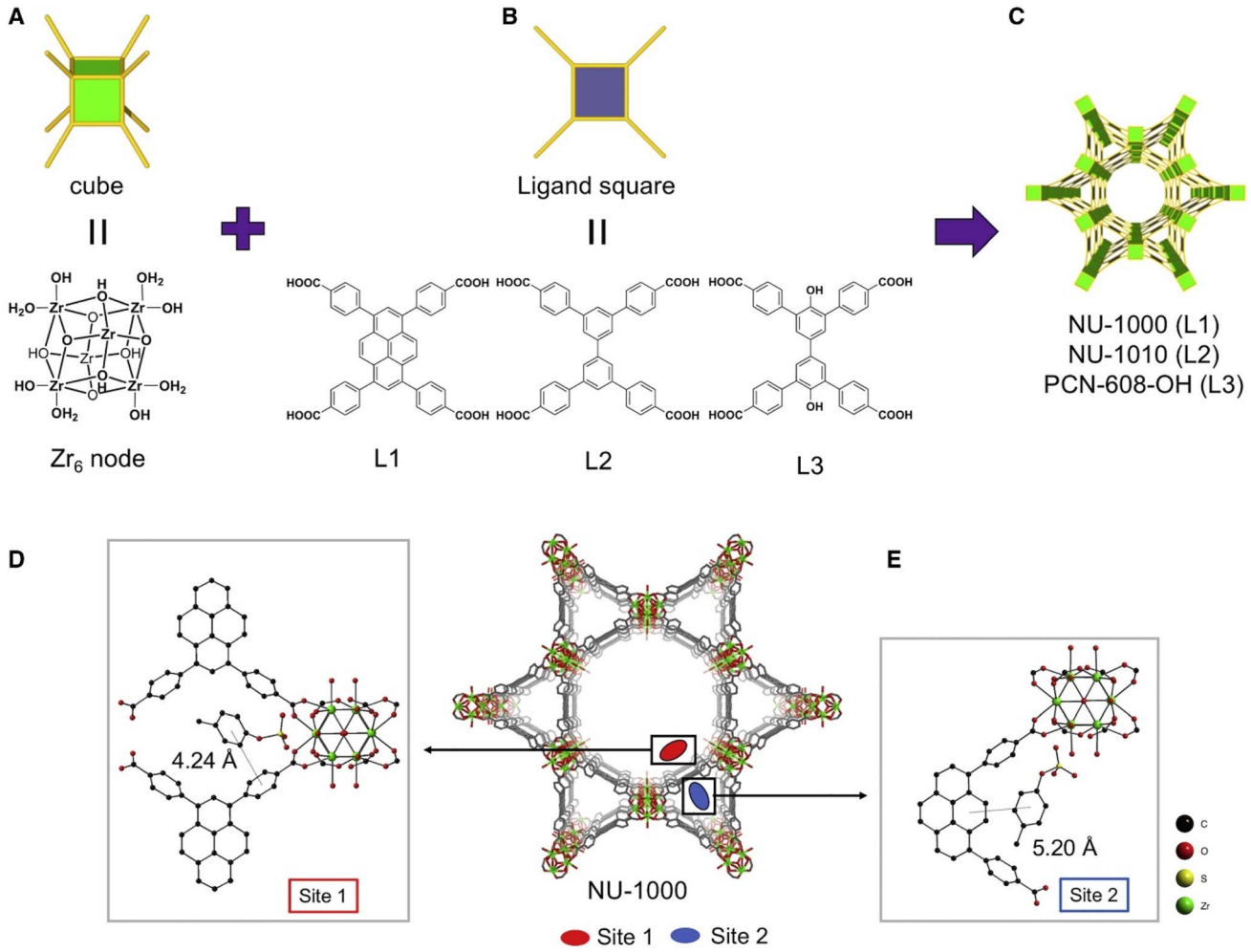

Fig. 7 Representation of isostructural Zr_6-based MOFs with **csq** topology showing (A) Zr_6 clusters and (B) tetratopic ligands. (C) Demonstration of the **csq** topology. Optimized geometries of *p*-cresyl sulfate (*p*-CS)-pyrene and Zr_6 clusters domains at both sites after *p*-CS adsorption at (D) site 1 and (E) site 2. Only one orientation of *p*-CS is depicted at each site for clarity, and potassium counter ions and hydrogens are not shown.[91] From ref. 91 with permission. Copyright 2020, Cell Reports Physical Science.

potassium *p*-CS and potassium IS onto **NU-1010** exhibits noticeably greater increases in entropy compared to adsorption in **NU-1000**, indicating the significant role of hydrophobic interactions in the adsorption at site 1. The error bars represent the standard deviations of triplicate measurements (Fig. 7).[91]

Stability of Zr-MOF in a wide range of pH is one of the most important properties of them. This is the main reason for using highly stable porphyrin-based MOF called **PCN-222** by Rezaei *et al.* for extract Hg^{2+} ions from fish samples with pipet tip method. Zhou *et al.* and Yaghi *et al.* first reported **PCN-222** independently with **csq**, (4,8)-connected topology and 3.7 nm hexagonal channels and 2220 $m^2\ g^{-1}$ BET surface.[89,90] The total pore volume of **PCN-222** is reported to be 1.3 $cm^3\ g^{-1}$. It was designed using meso-tetrakis(4-carboxyphenyl)porphyrin (H_2TCPP) and $Zr_6(\mu_3\text{-}OH)_8$ clusters. Rezaei *et al.* noted that the large pores of **PCN-222** facilitate the diffusion process and enhance connectivity among guest sites, making it an excellent candidate for coordinating heavy metal absorbents. Li *et al.* also reported the production of **PCN-222**, known as **MOF-545**, using the solvothermal method with formic acid as a modulator. They utilized it as an absorbent for various anionic and cationic dyes, studying their adsorption kinetic parameters. These dyes were employed to investigate properties such as the kinetics of adsorption (which followed a pseudo-second-order model) and thermodynamics. The ideal Langmuir model suggested that adsorption occurs as a process of achieving monolayer coverage and is governed by an exothermic enthalpy effect. The remarkable adsorption capabilities of **PCN-222** prompted researchers to develop a chromatography column for experimental use. Porphyrin frameworks, with or without metal ions, have been widely explored for various applications. Feng *et al.* reported **PCN-222(Fe)**, which exhibits peroxidase activity, while Chen *et al.* reported **PCN-222(Pd)** as a fluorescent "turn on" sensor.[113] The method reported by Li, which is also documented by Zhou *et al.*, involved two sonication steps and 80 hours of heating at 130 °C, in addition to the drying and activation processes.[114,115]

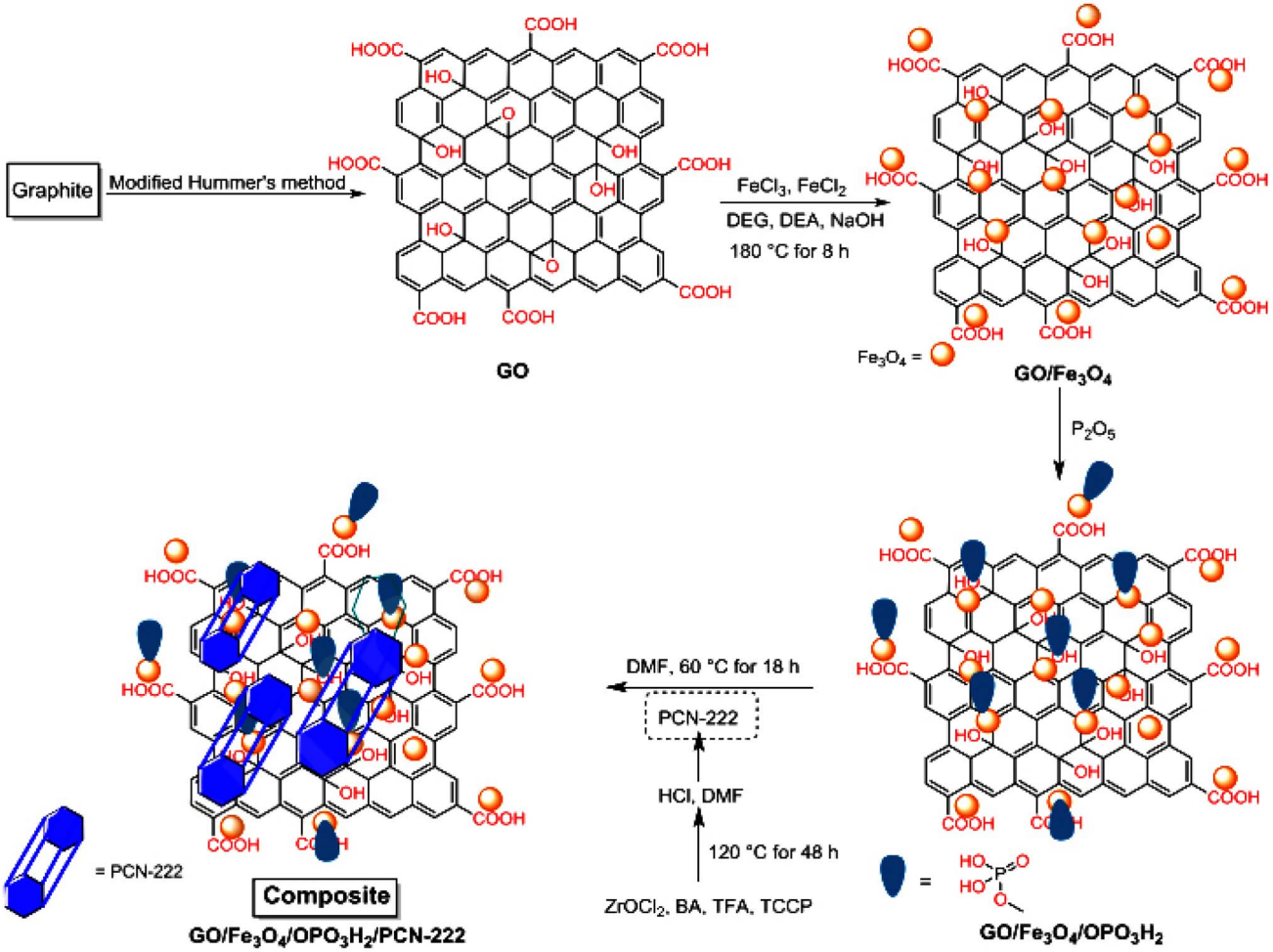

Fig. 8 Schematic representation of the synthesis pathway for the $GO/Fe_3O_4/OPO_3H_2$/PCN-222 composite. The process involves the stepwise functionalization of graphene oxide with iron oxide nanoparticles and phosphonic acid groups, followed by their incorporation onto the surface of the csq-topology Zr-based MOF, PCN-222. The resulting hybrid structure combines the high adsorption capacity of the functionalized nanomaterials with the porosity and selectivity of the MOF framework, enabling efficient uranium ion extraction from aqueous solutions.[116] From ref. 116 with permission. Copyright 2021, Elsevier.

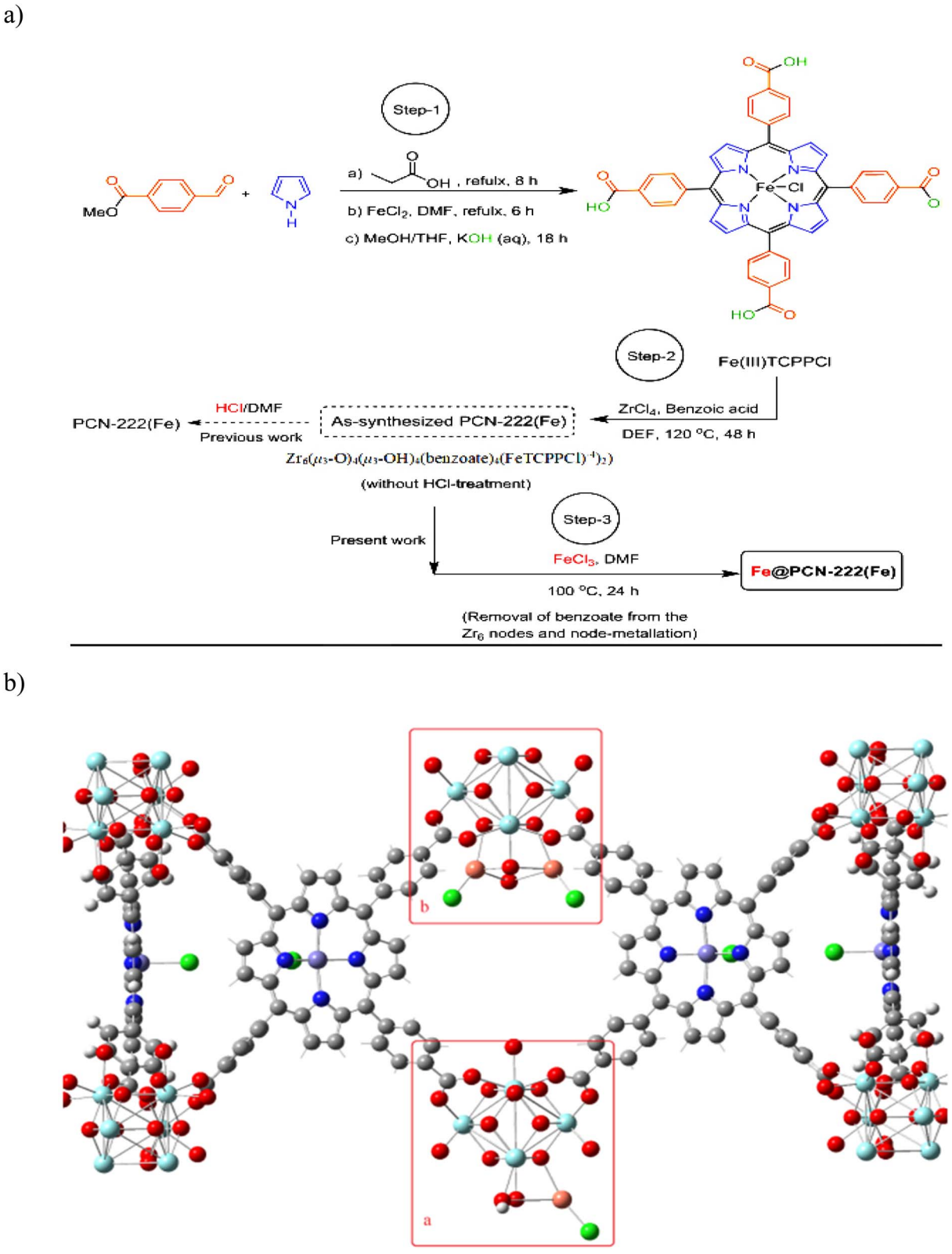

Fig. 9 Schematic representation of the incorporation of iron ions into the structure of PCN-222(Fe). (a) Stepwise synthesis of Fe@PCN-222(Fe), involving post-synthetic modification of PCN-222 with $FeCl_3$, leading to dual incorporation of iron atoms both in the porphyrin centers (Fe-TCPPCl linkers) and at the Zr_6 cluster nodes. (b) Proposed structural models of the resulting Zr_6Fe_2 node, illustrating the placement of iron(III) ions around the metal clusters. Pink spheres represent Fe ions and green spheres represent Cl^- counterions. This dual-metallic hierarchical MOF exhibits enhanced reactivity for visible-light photocatalysis and cooperative catalysis with earth-abundant metals.[117] From ref. 117 with permission. Copyright 2019, Elsevier.

Hariry *et al.* developed a new method for synthesizing **PCN-222/MOF-545** based on ultrasound, which exhibited superiority due to lower temperature and significantly shorter synthesis duration. They dissolved $ZrCl_4$ and MTCPP ligand in DMF with benzoic acid as a modulator under ultrasonic radiant power ranging from 600 W to 1200 W and temperatures between 40 °C to 120 °C for 120 minutes. Impurities were removed through a 24 hours washing process with acetone, followed by vacuum drying for 6 hours. Comparing the two methods, it was found that the crystals' morphology remained the same. Both methods demonstrated a type-IV absorb isotherm and a BET surface area of 2013.13 $m^2\ g^{-1}$. Samples synthesized with ultrasound exhibited two stages of weight loss: the first due to solvent elimination at 160 °C, followed by complete collapse between 300 °C to 600 °C. This data suggests that Hariry's method produces nearly identical results with significantly less energy and time. This newly synthesized MOF with porphyrin ligands can coordinate with different metals such as Mn^{3+}, Fe^{3+}, and Cu^{2+}, providing additional coordination sites for absorbent materials. This prompted a comparison of their absorption properties, crystallization yields, and adsorption capacity for various organic dyes. The results indicate that **PCN-222** with Cu^{2+} exhibited a stronger correlation with MB similar to **PCN-222-(Zr)**, while **PCN-222-(Mn)** demonstrated the highest adsorption capacity among different MOFs. However, Mn^{3+} and Fe^{3+} showed greater correlation with MO.[85]

Khajeh *et al.* successfully synthesized **GO/Fe_3O_4/OPO_3H_2/PCN-222** with a high-performance adsorbent on the surface of **csq**-topology Zr-based MOF in the way that showed in Fig. 8 presence of the GO/Fe_3O_4/OPO_3H_2 results a reduce of the surface area from 2249 to 1350 $m^2\ g^{-1}$. This composite was applied for distributive solid-phase uranium ions' extraction which dissolved in wastewater, based on critical parameters such as the amount of adsorbent, extraction and desorption times, pH of solution, and type and concentration of elution solvent that have been studied and optimized. Khajeh *et al.* reported the highest adsorption capacity of the adsorbent was determined to be 416.7 mg g^{-1}, much improved from what was reported with the individual components. The composite spectrum shows the characteristic adsorption bands related to the **PCN-222** MOF and GO. The adsorption band is attributed to GO's existence from 220 nm to about 260 nm. Besides, the adsorption band from 410 nm to about 700 nm conforms to the porphyritic MOF. All received data emphasize that the metal–organic framework was perfectly linked to GO/Fe_3O_4/OPO_3H_2 to achieve the formal hybrid material.[116]

Khajeh *et al.* in another study, have reported zirconium-iron(III) porphyrin MOF with hierarchically structured called **PCN-222(Fe).** Post synthetically modification was applied on **PCN-222** was with iron salts; this new modified MOF consists of $Zr_6O_6(OH)_8(H_2O)_2(Fe)_2$ clusters connected by Fe-TCPPCl linkers (Fe^{2+} coordinated to central place of ligands) and used as an extra efficient forerunner, to result a MOF which has 2types of metals (Zr, Fe) named as **Fe@PCN-222(Fe).** Fe ions are present in both ligands and nodes. The apply of $FeCl_3$ can ensue in both eliminating the benzoic acids, potentially attributable to the *in situ* generations of HCl, and remained eight unsaturated terminals containing –OH//H_2O ligands on the Zr_6-clusters for the metalation. At the end, the iron(III) atoms were decorated around metal clusters of **PCN-222(Fe)**, and a more reactive framework was obtained without using any post-treatment with a dilute hydrochloric acid solution as mentioned before. The

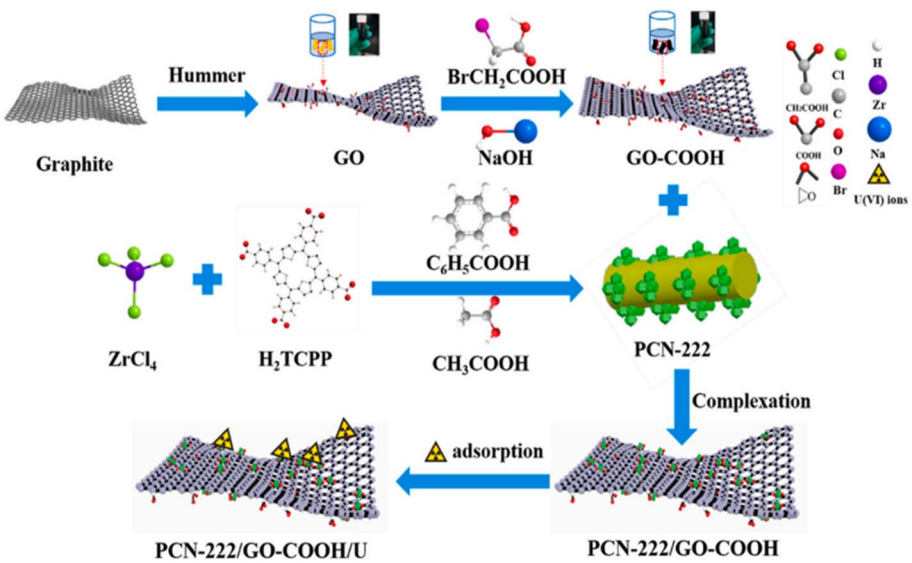

Fig. 10 Step-by-step schematic of the synthesis and assembly of the PCN-222/GO-COOH/U composite used for U(VI) adsorption. The process begins with the oxidation of graphite to graphene oxide (GO) *via* the Hummers' method, followed by functionalization with bromoacetic acid and subsequent carboxylation to yield GO-COOH. Separately, the Zr-based MOF PCN-222 is synthesized from $ZrCl_4$ and H_2TCPP in the presence of benzoic and acetic acids. The PCN-222 framework is then anchored onto the GO-COOH surface *via* complexation to form the hybrid PCN-222/GO-COOH composite. This material is subsequently employed for the selective adsorption of U(VI) ions from aqueous solutions. The composite exhibits exceptional thermal, chemical, and structural stability, retaining the porphyrinic framework of PCN-222 while enabling efficient U(VI) recovery from real wastewater.[118] From ref. 118 with permission. Copyright 2021, Elsevier.

mesoporous MOF after modification could be used directly as (photo)-catalyst and not provide any damage to structure. This study exhibits the possible usage of multifunctional MOFs involve cooperative reactions that combine visible-light photocatalysis and earth-abundant metal catalysis. To be more understandable, an economically viable and environmentally benign process renders it more suitable for the continuous production of chemicals (Fig. 9).[117]

PCN-222/GO-COOH composites were subjected to boiling water, DMF, strong acid, or base at room temperature for 24 hours to check their stability. TGA results showed that **PCN-222/GO-COOH** composites exhibited excellent thermal stability. These test results demonstrated the outstanding thermal, physical, and chemical stability of the composite. Bi *et al.* utilized this composite for U(VI) recovery from real U(VI)-containing wastewater, as discussed above by Khajeh *et al.* The distinguished selectivity, removal rate, and adsorption capacity of the **PCN-222/GO-COOH** composites make them suitable candidates for recovering U(VI) from real U(VI)-containing wastewater. TEM and TEM-EDS images captured from **PCN-222** illustrate a normal tubular-like structure with a diameter of about 2.3 μm, exhibiting precise and uniform crystal lattices at higher magnification and uniform distributions of elements N, C, O, and Zr in the **PCN-222**. The step-by-step preparation of the absorbent is shown in Fig. 10. After complexing with GO-COOH, **PCN-222** was successfully loaded onto the surface of GO-COOH, and the coating occurrence was observed at higher magnification, indicating that the original structure of **PCN-222** was preserved in the complexation process.[118]

Modification of **PCN-222** once again has been chosen as the subject of the study of Khajeh *et al.* Thiol-functionalized **PCN-222** (**PCN-222-MBA**), was developed as an adsorbent using a SALI method, an acid–base reaction between molecule 4-mercaptobenzoic acid and terminal –OH/–H_2O groups on Zr_6-nodes of **PCN-222** to functionalize mesoporous **PCN-222** for gold ionic adsorption in the aqueous environment.[119]

He *et al.* focused on a modulator-based strategy for tuning the pore environment and mesoporous channels to achieve a structure with excellent catalytic activity, which serves as the gathering place of the MOF catalytic center. The size of the mesoporous channels is 2.8 nm, and although these long-range channels are not visible in the TEM image, they concluded that the environment around the cavity might vary. The mesoporous nature of the MOF, similar to **PCN-222** (**csq**, (4,8)-connected), was determined by SAXS studies. The N_2 adsorption isotherm is type IV, indicative of a mesoporous structure, with a range of 0.6 to 2.5 nm referred to as the hierarchical structure. NMR studies were conducted to understand the effect of modulators in the cavity environment, such as water and monocarboxylic acids. WM-MOFs, based on their design, exhibited excellent catalytic performance in the cycloaddition reaction of CO_2 and different epoxides, with high selectivity and conversion, and at low temperature and pressure. The effects of modulators (like water and monocarboxylic acids), as shown in this study, may explain why WM-MOFs exhibited higher weight loss and a lower decomposed temperature.[84]

It is evident that structures with **csq** topology have garnered considerable attention in research. However, it's essential not to overlook the fact that researchers are often drawn to working with structures that have been extensively studied rather than newer, less explored ones. The significance of this point can be carefully evaluated through subsequent studies conducted by various researchers and the conclusions drawn from these collective efforts. The **csq** structure renders the material suitable for applications requiring dual adsorptions of different molecules, as well as scenarios where the material needs to traverse units added to the MOF post-synthesis. The presence of two types of channels in the **csq** structure not only introduces new functional units but also makes it suitable for catalytic and absorption purposes. Nonetheless, the lack of uniform channels in the network has prompted researchers to explore other systems. It's worth noting that the realm of metal–organic frameworks (MOFs) is relatively new in scientific discussions, and comparative studies are common due to the variety of structures employed for similar applications.

2.3 scu topology

This topology provides uniform channels with 8 connected clusters and 4 connected organic nodes, so the same Zr precursor and same ligand which produced the **csq** topology also could play a role in creating this topology (Fig. 11 and 22). The **scu** topology, like the **csq** topology, is among the most important and frequently observed topologies for zirconium-based metal–organic frameworks (MOFs). While these two topologies share many similarities, such as the hexanuclear zirconium cluster ([Zr_6]) as the central metal node and their comparable high porosity, they also exhibit distinct differences. In **csq**, the nodes are connected to linkers in a (4,8)-connected fashion, whereas in **scu**, the connections follow a (6,6)-connected pattern. These simpler connections in the **scu** structure result in more straightforward and homogeneous pores, as illustrated in Fig. 11. The **csq** topology typically forms

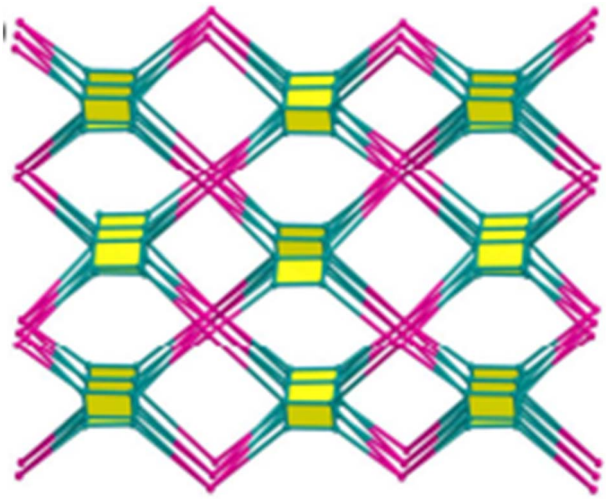

Fig. 11 Schematic of **scu** topology.[137] From ref. 137 with permission. Copyright 2018, American Chemical Society.

mesoporous channels with larger diameters, while **scu** channels are generally smaller and more uniform. This topology clearly creates more uniform cavities. **scu** MOFs are often utilized in applications requiring higher structural stability and more consistent diffusion properties.

NUPF-1 is one of the members of MPFs (metal porphyrin frameworks) with $Zr_6(\mu_3\text{-}O)_4(\mu_3\text{-}OH)_4$ clusters similar to **PCN-225** with **scu**, (4,8)-connected topology[50,98] reported by Xu *et al.* Until then this topology was unprecedented, they reported this MOF with doubly interpenetrations which has high thermal and chemical stability and undeniable flexibility. MPFs had wide application in optical perception systems, gas storage, and catalysts. Thus **NUPF-1-RuCO** was synthesized using $[Ru_3(CO)_{12}]$ and the product was used for catalysis amination of alkanes with azides. Central metal in MPFs had a great effect on their property, for example, Wang *et al.* reported low catalytic activity toward epoxidation of *trans*-stilbene for **MMPF-5(Cd)** but changing Cd^{2+} to Cu^{2+} improved its catalytic performance.[120] **NUPF-1** has rod-shape purple crystals obtained by solvothermal reactions of a porphyrin ligand with $ZrOCl_2 \cdot 8H_2O$ in DMF and formic acid as a modulator. The porphyrin ligand is core-free and almost planar and also tetraphenyl porphyrin and benzoic acid moieties linked by amido units, with a span of 2.4 nm between the two neighboring carboxylate groups. Hence, the structure contains 8 connected octahedral nods and 4 connected D_4h organic nods. Eventually, **scu** topology with 2.3 × 5.1 nm was obtained. 73.6% of MOF was free space, and its large meso channel gives this opportunity for a twofold structure which was created and the only meso channel divided into 4 smaller channels with 2.66 × 1.78 nm, 2 × 0.72 nm, and 1.91 × 0.67 nm windows **NUPF-1** is strongly thermal and mechanical stable; TGA collapse temperature is 450 °C, and can tolerate pressure up to 12.5 Ton per cm^2. It also showed high chemical stability; its pore volume didn't change in pH equal to 0.7 and 9. **NUPF-1** could absorb 107 $cm^3\ g^{-1}$ of ethanol, 154 $cm^3\ g^{-1}$ of methanol, and 182 $cm^3\ g^{-1}$ of water in the vapor phase too, which clearly shows a high desire to absorb polar material. Another study talked about catalytic function of **NUPF-1-RuCO** and its size selective property in reactions.[94]

NU-1000, with the **csq** topology, emerged as a promising candidate for various absorption-based applications. Verma *et al.*, while investigating the structural features of **NU-1000**, reported the existence of another scu-net polymorph, **NU-901**. This polymorph possesses a smaller average pore size and volume compared to **NU-1000** and is not considered mesoporous, as also noted by Garibay *et al.* Its application in enhanced CO_2 adsorption was investigated.[121] Goswami *et al.* used time-resolved fluorescence imaging to identify this impurity as a structural isomer present at the center of the crystallites. They also mention that the type of modulator has an effect on the amount of this impurity. The **scu**-net structure of **NU-901** features 1.2 nm diamond-shaped channels. In their study, they present some methods for limiting the production of **NU-901**, such as using biphenyl-4-carboxylic acid as a modulator or a comodulator like TFA.[93] Although both **NU-901** and **NU-1000** are produced as impurities in another production process, phase-pure samples of both MOFs have been successfully synthesized in bulk and investigated for electrocatalysis and separation membranes. Self-assembled monolayers and crystal engineering were utilized to control the polymorphism and orientation of **NU-901**/**NU-1000** thin films, as shown in Fig. 12. The microspore width for both **NU-901** and **NU-1000** is almost balanced. However, owing to the presence of modulators occupying free sites of the cluster, the mesopores are smaller than reported. A washing step with HCl to remove modulators resulted in larger mesopores, approximately 30 Å. It was assumed that increasing the density of Zr-oxo clusters on the functionalized FTO can control the nucleation density of **NU-1000**. It can be inferred that the functionalized FTO possesses a surface coating of compact carboxyl groups (−COOH), mainly due to the ability of 16-PHDA to form a dense layer of carboxyl groups (−COOH) on the ITO surface.

As a different synthetic pathway from what was explained previously, presoaking the SAM-altered FTO substrate in the Zr-oxo cluster solution before the solvothermal synthesis enables a dense formation of Zr-oxo clusters on the substrate, leading to a high nucleation density in **NU-1000**.[122]

Using TTFTB (tetrathiafulvalene tetrabenzoate) and Me-TTFTB (tetrathiafulvalene tetramethylbenzoate) ligands along with Zr_6 clusters, Su *et al.* reported two different MOFs with the following formulas: $[Zr_6(TTFTB)_2O_8(OH_2)_8]$ and $[Zr_6(Me\text{-}TTFTB)_{1.5}O_4(OH)_4(C_6H_5COO)_6]$. Through steric tuning of the ligands, they achieved two distinct MOF structures. TTFTB leads to 4-connected square planar nodes, whereas Me-TTFTB results in 8-connected cubic nodes. This results in a 4,8-connected **scu** topology with TTFTB and a 4,6-connected she topology with Me-TTFTB.

Zr-TTFTB, which exhibited higher connectivity, showed micropores with a consistent pore size of about 12.7 Å. On the other hand, **Zr-MeTTFTB**, with lower connectivity, provided hierarchical pores with micropores measuring 12.6 and 15.8 Å, along with mesopores of 20.7 Å. The entire N_2 absorption and

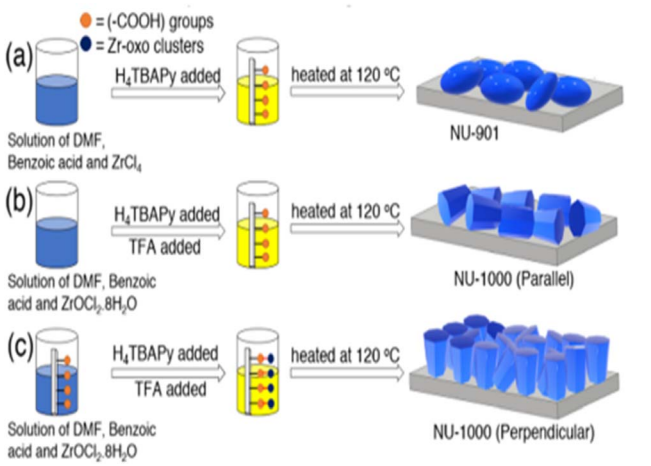

Fig. 12 Synthesis process to solvothermally produce films of three product (a) **NU-901**, (b) **NU-1000** with parallel and (c) perpendicular orientation.[122] From ref. 122 with permission. Copyright 2021, American Chemical Society.

BET surface area reached 536 cm^3 g^{-1} and 1932 m^2 g^{-1}, respectively, with type-IV isotherms. However, **Zr-TTFTB** exhibited a type-I isotherm with an entire N_2 absorption of 393 cm^3 g^{-1} and a BET surface area of 1353 m^2 g^{-1}, indicative of a typical microporous structure.[98]

Thus **scu** topology is another channel-oriented topology in which all channels are uniformly placed. In this topology, ligands and metal nodes are identified hypothetical cylinders within, making a good position for a flow of materials inside. In this topology, the channels can be square or rhombic, meaning that the vertical diameter and the horizontal diameter can be different or equal to each other. This topology has been studied more for absorption purposes, especially for gas absorption in the history of MOF uses. The lack of cages in the structure has made this topology inappropriate for loading applications or applications that require the fixation of a foreign substance inside the MOF.

2.4 ftw topology

ftw topology is commonly produced when square/rectangular-shaped tetracarboxylates are coordinated to Zr_6 clusters. Unlike previous topologies, here we have a cluster with more connectivity (12 *vs.* 8), and regardless of the size of the ligand, we should see smaller cavities. A 12-connected Zr_6 cluster ideally connected to a square or rectangular linker, and commonly did not provide mesoporous MOFs.[72]

MMU is a Zr-based MOF based on BDC^{2-} with 200 nm crystals in average, relatively low 453.8 m^2 g^{-1} BET surface area, pore size between 3.5 to 7 nm, and **ftw** topology used by pang *et al.* for immobilizing laccase. They reported this MOF could accept 221.84 mg g^{-1} of bovine serum albumin (BSA) in its pores. After that, the enzyme showed more stability in a wider range of pH and higher repeatability than the free enzyme. An interesting point about **MMU** is that its pores did not block in high concentration of enzyme; its structure allows the material to penetrate the pores structure after enzyme is encapsulated. For design of **MMU**, a surfactant-templating method that was previously used for silica gel to become mesopores was used. Chelating agent and surfactant added to the reaction caused developing of hierarchical structure. Pang *et al.* applied TFA as a modulator and CTAB (cetyltrimethylammonium bromide) as a chelating factor and small amount of hydrochloric acid.[86]

Li *et al.* proposed a novel MOF with a pore size ranging from 3.8 to 4.5 nm and **ftw** topology, utilizing it for encapsulating and immobilizing a nerve agent known as OPAA. Previous attempts to enlarge the pore and aperture size of **NU-1000** by introducing C–C single or triple bonds between adjacent phenyl rings resulted in the formation of an isomorphic zirconium MOF with the **ftw** topology. In response to this challenge, they developed a tetra-carboxylate pyrene-based linker, using DMF as the solvent and trifluoroacetic acid as a modulator to produce **NU-1003** with the same topology as **NU-1000**. Two types of pores were identified: 4.4 nm hexagonal and 1.7 nm triangular pores, showcasing an example of designing ligands to achieve the desired topology. This also demonstrates how altering and adding new lateral arms to ligands can impact the topology.[102]

Wang *et al.* during research on methods for separating ethylene gas from a mixture of gases, achieved new metal–organic frameworks called **UPC-612** and **UPC-613** that are modified version of **ftw**-based **MOF-525** (first reported by Yaghi *et al.* in 2012 (ref. 123)) with Zr_6 clusters. Two new ligands called H_4L-L and H_4L-S has been used to product **UPC-612** and **UPC-613**. These linkers were functionalized with a cyclopentadiene cobalt functional group which increases the host–guest interaction and achieves efficient ethylene purification. They reported BET surface area of **UPC-612** and **UPC-613** BET are 2016 and 853 m^2 g^{-1}, respectively. The adsorption enthalpy order (Q_{st}) at zero coverage is C_2H_2 (23.9 kJ mol^{-1}) > C_2H_6 (22.4 kJ mol^{-1}) > C_2H_4 (16.9 kJ mol^{-1}); in summary, **UPC-612** separate C_2H_2 and C_2H_6 from C_2H_4 compared to **MOF-525** and the version that only modified by cobalt (MOF-525(Co)) uniquely, creates a substance with a purity percentage higher than 99.99%. Irregular cubes surrounded by six linkers presented in this MOF, have approximately 2 nm diameter of the cage and this feature enables modifications. Within a cage structure, the metal cluster is situated at the vertex, and the linker covers the surface of the cube, distinguished from the pore structure in which guest molecules cross through the cage; they need to enter through the cage window. Irregular movements are then made in the cavity and finally out of another cage window. They reported information on the mechanism and how to increase the separation capacity in their study.[96]

The orientation of π-interaction sites in a sequence of synthesized and evaluated MOFs, specifically **MOF-526**, **MOF-527**, and **MOF-528**, has been documented. These MOFs display a systematic increase in pore size, ranging from 1.9 nm in **MOF-526** to 3.7 nm in **MOF-528**, as well as enhanced permanent porosity and capability to incorporate and subsequently release extended organic materials in water. The trapped organic material, which has a polycyclic structure, and the π-interaction between discrete porphyrin units in the MOF structure, contribute to remarkable reversibility. Additionally, the mesopores in these MOFs facilitate rapid adsorption kinetics. In particular, these MOFs, through their porphyrin units, enable the quantitative absorption of various large organic dyes (details provided below) in a 2 : 1 molar ratio, showcasing unique kinetic behavior for MOFs, such as a concentration of 4.54 × 105 mol L^{-1} for rhodamine B (RhB) at very limited water concentrations of 10 ppm. Rotational-echo double-resonance (REDOR) NMR experiments exposed the interval between the entrapped molecules and the porphyrin units in the ligand, ranging from 3.24 to 3.37 Å, confirming the specific π-interaction. Ten complete inclusion–release cycles were successfully conducted in these MOFs, demonstrating their reversible and repeatable dynamics without any decomposition, making them highly suitable for recycling large polycyclic hazardous molecules from water. **MOF-526**, in particular, performs on par with leading-edge carbons and polymers. In contrast, this study introduces planar porphyrin-based linkers that are extended, with the largest organic linker spanning approximately 45 Å, effectively utilizing both sides of the flat porphyrin unit for interactions with organic guest molecules through specific π-interactions. While a broad range of applications for porphyrin-

based MOFs, including catalysis and the absorption of gases and macromolecules, has been extensively explored, this is the inaugural study demonstrating their capability to quantitatively interact with prominent organic guest molecules using specific π-interactions for water and wastewater treatment. This characteristic, combined with their exceptional chemical stability, positions these MOFs as ideal candidates for kinetic recyclability and the removal of typical organic pollutants from water, challenging the latest advancements in carbons and polymers. Finally, the smallest member of this isoreticular group, **MOF-525**, is a chemically stable microporous MOF created by connecting 12-connected zirconium oxide clusters $[Zr_6(OH)_4O_4(-CO_2)_{12}]$ with a porphyrin linker (tetrakis(4-carboxyphenyl) porphyrin), known as H_2-TCPP, which has a square planar shape. To construct the larger members of this series, benzene or phenylene units are incorporated into the TCPP linker between the carboxylate and porphyrin π-interaction site. This not only aids in purifying the linker during its synthesis but also ensures the reversibility necessary for the growth of the corresponding MOF crystals.[108] Each extended MOF variant in this series maintained the fundamental cubic **ftw** topology. The strategic placement of the porphyrin unit at the center of each cubic lattice face ensured optimal separation of the π-interaction sites, facilitating dynamic and reversible interactions with guest molecules. The use of larger linkers led to an increase in the pore sizes of the MOFs from 2.0 to 4.5 nm, enhancing the efficacy of the π-interaction sites. This structural arrangement ensured that the porphyrin π-interaction sites were well-isolated within their crystal frameworks, allowing guest molecules complete access to the pores. The MOFs demonstrated type IV isotherms during N_2 adsorption studies, with surface areas recorded at 4260, 2000, and 3550 $m^2\ g^{-1}$, respectively. Given their exceptional chemical stability, lasting porosity, and

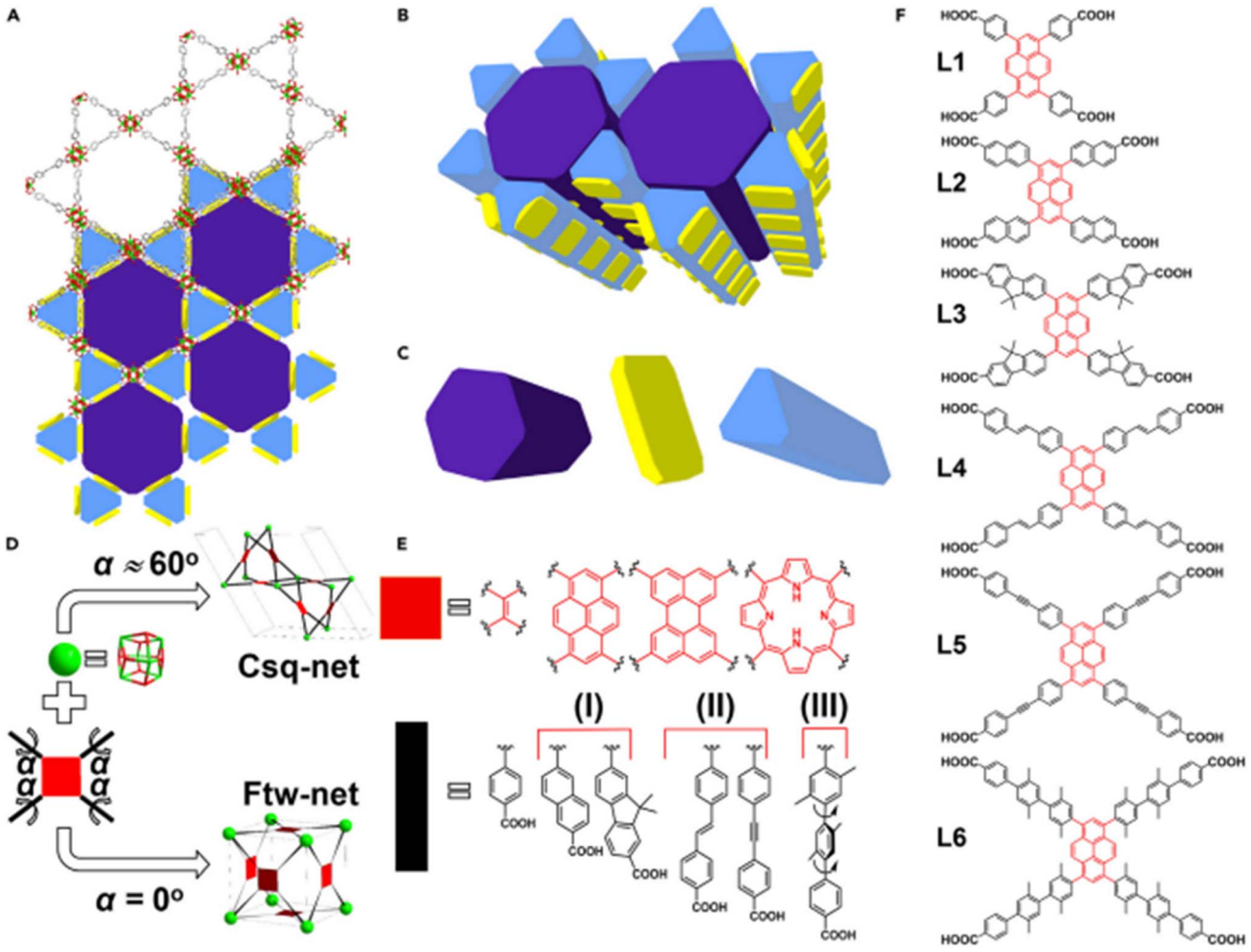

Fig. 13 Schematic presentation of **csq**-net topology and design of linkers for **csq**-net Zr-MOFs (A) Top view and (B) side view of interconnected hierarchical channels composed (C) channels structure shown by the geometric shapes marked in fig in **csq**-net Zr-MOFs. (D) Relationship between intramolecular torsion angles of the linkers and the topology of the resulting product (Zr_6 clusters illustrated by green balls). (E) Existing and proposed chemical structures of the tetratopic linkers were composed of different backbones (red squares) and arms (black rods) used for constructing **csq**-net zirconium MOFs with varying carbon chain. (F) Chemical structures of linkers L1–L6 used for constructing NU-100*x* ($x = 0$, 3, 4, 5, 6, 7) series MOFs.[90] From ref. 90 with permission. Copyright 2019, Royal Society of Chemistry.

substantial pore openings, these MOFs are perfectly suited for demonstrating consistent and reversible behavior in water.[87]

Lyu *et al.* reported another study on extending novel MOFs *via* linker functionalization. In this research, three distinct Zr-based MOFs were synthesized by controlling the steric aspects of the conformations of replaced tetratopic carboxylate linkers. They realized that topology could simply be related to the linker conformation adjustments. Factors affecting linker conformation is modulating reagent, concentration, metal precursor, environmental factors, and solvent. Using tetratopic linkers which provide high rotational freedom for their lateral arms like tetracarboxyphenylporphyrin (TCPP) may make various topologies.[113,124] In recent studies by this group on the production of **csq**-net MOFs, they unexpectedly obtained MOFs with **ftw** topology instead of those with larger ligands. They proposed that a critical influence of the planar "backbone" and the arm's torsion angle was the reason for this observation. They suggested that when the torsion angle was close to 60°, the **csq** topology prevailed, while a torsion angle close to 0° resulted in the **ftw** topology (see Fig. 13). Density functional theory (DFT) calculations indicated that pyrene-aromatic systems tend to form 50–60° torsion angles around their minimal energy, providing insight into why researchers are encouraged to investigate linkers of this family to produce **csq** structures.[66]

Three linkers were designed to introduce to increase the rigidity of the structure (Fig. 13). With L1 linker **NU-903** was formed (first reported with the name of **CAU-24** by Stock *et al.*[125]) with a **scu** topology. With L2, **NU-904** is obtained, featuring oval-shaped crystals. The crystal properties of **NU-904** reveal a unique reticular-merohedral twin configuration, where three distinct orientations are stacked along the *b*-axis, each rotated 60° relative to the others. This arrangement forms a rare 4,12-connected **shp** structure, representing the mean structure of the threefold twinned **NU-904**. The interplay of three **scu**-net components in the reticular twins contributes to the overall 6-fold symmetry observed in the structure. Notably, the presence of threefold twins in the ordered 4,8-connected **scu** structure results in a twinned version of the rare **shp** structure. This intrinsic connection between the two topological networks was previously undocumented before Lyu's investigation. Their findings also reveal channels with a triangular configuration, contrasting with the diamond-shaped channels identified in **NU-903**.[90]

ftw topology, like the other topologies mentioned before, is based on four connected linkers. Due to the higher connectivity of this topology compared to the previous ones, structures containing this topology are usually classified as microporous materials. Researchers enlarged the linkers, in order to reach mesoporous materials, and the use of peers usually leads to the creation of **csq** and **scu** topologies. Unlike the topologies before, **ftw** topology is based on cages and no channels are observed. As explained, this topology is mostly used for encapsulation or in reactions requiring, more and more frequent collisions; so we use them to stay for a longer time in the structure. Since the flow of molecules entering this structure must pass through one cage window and then leak from another window to the adjacent cage, such placement helps materials including this topology become very suitable for absorption and encapsulation purposes. As discussed earlier, the **ftw** topology exhibits higher connectivity. This topology emerges when fewer modulators are used during synthesis. The high connectivity leads to the formation of smaller pores. Conventionally, employing smaller ligands in this topology results in non-mesoporous structures. The **ftw** topology also features higher symmetry and lacks a hierarchical structure. While **scu** and **csq** topologies are commonly used for applications such as gas adsorption and encapsulation, topologies like **ftw** and **rtl** are designed for more specialized applications or specific conditions.

2.5 fcu topology

It is not wrong to mention that **fcu** was the first topology reported and investigated in Zr-based MOFs. The first reported Zr-based MOF was **UiO-66**, reported by Cavka in 2008.[46] The **UiO-66** structure consists of octahedral cages and tetrahedral cages, designed with slight triangular windows with a diameter near 0.6 nm (Fig. 14). **UiO-66** is the first reported Zr-based MOF that has suitable stability and its and other derivatives of this compound's remarkable properties studied a lot even until now,[126] but it has tiny pores with low surface area. **fcu** topology includes a 12-connected Zr_6 cluster connected toward ditopic ligands like BDC in **UiO-66**, BPDC in **UiO-67**, and TPDC in **UiO-68**.[127,128] Using **UiO-66** and **UiO-66-NH$_2$** treated with C_2F_5 and CF_4 plasma is a novel approach to develop hierarchical MOF networks. One of the positive features of **UiO-66** is its stability against moisture and acids, while its negative feature is the difficulty of electrical charge transfer. Additionally, its pore size is too small. Therefore, Decosta *et al.* developed a mesoporous MOF based on **UiO-66** as a template. The results of the reaction with different powers of the ultrasonic systems are correlated with the duration of treatment: (1) reducing the power level to 75 W increased the N_2 uptake by achieving the highest etching efficiency, and (2) it increased the cavity size and BET surface area while using **UiO-66**. In this study, fluorocarbon radicals were used to break Zr–O bonds, providing an excellent method to achieve the **fcu** topology with larger pores with 4,4′-biphenyl-dicarboxylate (BPDC) and terphenyl dicarboxylate (TPDC) as a linker.[129]

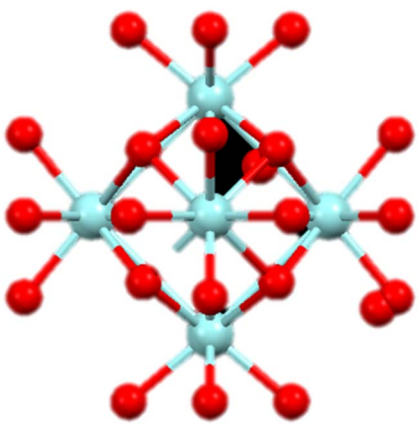

Fig. 14 Structure of UiO-66 node.

UiO-66, besides its importance as the first Zr-based also, plays a touchstone in comparisons, as we will see in the following. Kim *et al.* used three different absorbents (to separation of SF_6 gas from a mixture of SF_6 and N_2 **UiO-66**, **UiO-67**, and zeolite-13x). **UiO-67** (first reported by Cavka *et al.* at 2008) is a mesoporous MOF that, forasmuch as its bigger pore size than **UiO-66** showed better results in the separation process while both had **fcu**, 12-connected topology. **UiO-67** has a bigger pore size that was confirmed by type (IV) BET adsorption and had the highest selectivity in high pressures. At low pressures, the order of selectivity for 50/50 and 10/90 compositions was as follows: **UiO-66** > zeolite-13x > **UiO-67** (contrary to what was said at high pressure). SF_6 uptake at low pressures is precisely the opposite correlated with the order of the smallest pore size of the adsorbents. Results clearly indicate the superior SF_6/N_2 in 50/50 and 10/90 compositions separation performance of **UiO-67** compared with **UiO-66** and zeolite-13 under dynamic mixture flow conditions.[130]

The topology of **Zr-UiO-66-PDC**, which is one of the precursor materials for the preparation of **[Zr-UiO-66-PDC-SO_3H]Cl** that could be used for the preparation of dicyanomethylene pyridines *via* chemical and electrochemical methods, has been studied by Waitschat *et al.*[131] **[Zr-UiO-66-PDC-SO_3H]Cl** contains 12-connected Zr clusters with **fcu** topological network. [Zr-UiO-66-PDC-SO_3H]Cl is introduced as a mesoporous catalyst.

Lee *et al.* demonstrated an innovative method for converting microporous **UiO-66** into an amorphous mesoporous absorbent resistant to extreme pH and intense nucleophile challenges. **UiO-66** can function as an adsorbent in an acidic environment. It has been observed that it can absorb copper(II) and nucleophiles. However, its ability to maintain adsorption capacity despite the loss of its crystalline structure under the influence of nucleophiles at high or low pH indicates that its adsorption capacity does not depend solely on surface area or crystal structure. The disappearance of crystals occurs when it is immersed in acidic and nucleophilic conditions (0.1 M/1 M HCl/Cl^-, HNO_3/NO_3^-, H_2CO_3/CO_3^{2-}, H_3PO_4/PO_4^{3-}, and $HOAc/OAc^-$ at pH 1, 7, and 12, as well as in 0.1 M NaOH). As part of this pivotal study, adsorption kinetic tests of Cu^{2+} ions were conducted using pristine and modified **UiO-66** with 4 mg mL^{-1} adsorbents and an initial Cu^{2+} concentration of 9.6 mg L^{-1}, shaken at 200 rpm and 25 °C for 24 hours. Table 2 presents the effect of treatment.

Table 2 The BET surface area of anion-modified UiO-66 under different pH (ref. 132)

Sample	pH = 1	pH = 7	pH = 12
Pristine UiO-66	809.4		
0.1 M chloride	854.0	839.1	116.1
1 M chloride	479.2	349.1	6.5
0.1 M nitrate	737.6	527.3	727.3
1 M nitrate	400.4	281.2	18.5
0.1 M phosphate	9.7	12.3	28.8
1 M phosphate	5.3	3.6	9.9
0.1 M acetate	659.6	686.7	108.8
1 M acetate	428.7	31.8	33.3
0.1 M NaOH	148.0 (pH 13)		

The importance of the **fcu** topology is mostly summarized in its role in the history of zirconium-based MOFs. According to investigations and studies by various authors, this topology has been predominantly explored in the context of **UiO-66**. It is based on 2 and 12 connections, resulting in small pore sizes, yet a hierarchical structure is observed. Most studies have focused on **UiO-66** and its derivatives, as researchers aim to enhance this compound as the first zirconium-based MOF introduced.

2.6 spn topology

MOF-808 which is reported by Furukawa and co-workers, is made of tetrahedral cages with inorganic SBUs at its vertices and the 1,3,5-BTC linkers at its faces.[32] In this MOF, six formate ligands complete the coordination of the Zr cluster, which causes a **spn** topology with an internal pore diameter of 1.8 nm for the **MOF-808**. Furthermore, it makes surface areas higher than 2000 $m^2\ g^{-1}$. According to the official description of IUPAC

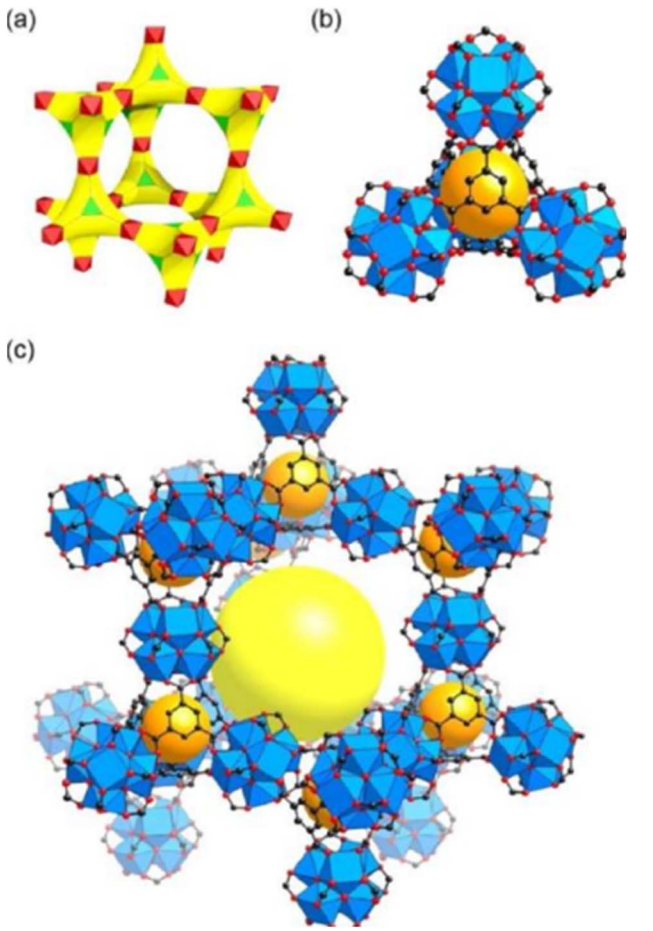

Fig. 15 Schematic of the spn topology (a) exhibited by MOF-808 with two kind of cages, first octahedral which indicate with red, and triangular which showed with green. (b) and large adamantane pores (c) atom color scheme: black for carbon, red for oxygen, blue for Zr. H atoms are hidden for better understanding. Large yellow and small orange balls showed the space in the framework.[133] From ref. 132 with permission. Copyright 2015, Wiley-VCH.

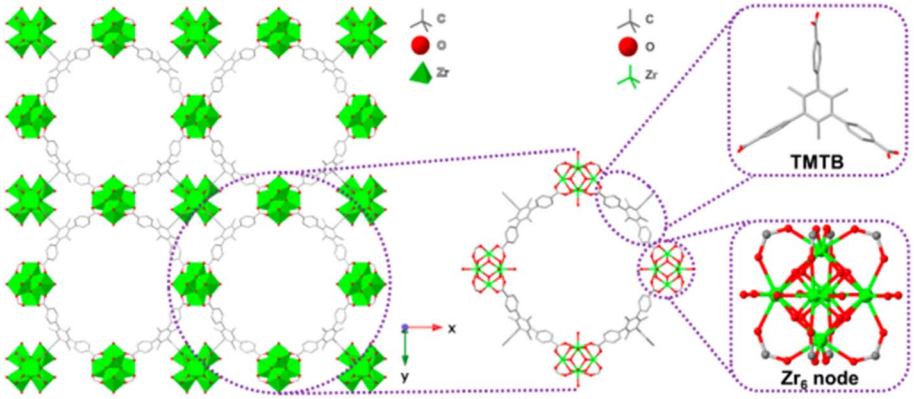

Fig. 16 Crystal structure and topology of the mesoporous Zr-based MOF **NU-1200**. The framework is constructed from 8-connected Zr_6 nodes with the formula $[Zr_6(\mu_3\text{-}O)_4(\mu_3\text{-}OH)_4]^{12+}$ and tritopic organic linkers, 4,4′,4″-(2,4,6-trimethylbenzene-1,3,5-triyl)-tribenzoic acid (TMTB). **NU-1200** exhibits a hierarchical pore architecture consisting of 1.4 nm sodalite-like cages and 2.2 nm interwoven mesoporous channels. Insets show the molecular structure of the TMTB linker and the Zr_6 node. The presence of four terminal –OH/H_2O groups per cluster provides accessible metal grafting sites, making **NU-1200** a suitable platform for post-synthetic metalation and catalytic applications.[140] From ref. 139 with permission. Copyright 2021, American Chemical Society.

MOF-808, is not a mesoporous MOF, but because the very small distance between its dimensions and definition of mesoporous material and the fact that **MOF-808** and **PCN-777** are the only examples for **spn** topology, authors dealt with it very briefly.[133] The **spn** topology is distinct from the previously discussed topologies. In the **spn** topology, the nodes are connected in a (4,6)-fashion, resulting in small yet orderly channels. Unlike **csq**, there is no hierarchical structure observed here. Due to its small and uniform pores, the **spn** topology is well-suited for applications requiring the adsorption of small gases and material storage. Similar to **scu**, **spn** also exhibits high symmetry, in contrast to **csq** (Fig. 15).

2.7 reo topology

Nowadays, one of the most exciting fields of study involves the substitution of metals in synthesized MOFs, as explored in Gharevand *et al.*'s research. They introduced Ce metal into Zr-based nets of **UiO-66** with **fcu**-12 connected topology, **DUT-67** with **reo**-8-connected topology, and MOF-808 with **spn**-6-connected topology to create heterometal clusters. Their aim was to investigate the catalytic activity of these clusters in the conversion of diisopropylfluorophosphate to its alcohol derivative. The study revealed that increasing the Ce/Zr molar ratio and doping trace amounts of magnesium enhanced the catalytic rate of P–F bond cleavage. Previous studies by Plonka *et al.*, Peterson *et al.*, and Mondloch *et al.* have also investigated these MOFs, yielding promising results.[134–137] As we know, Zr^{4+} is a strong Lewis acid, which has been the main focus of attention in Zr-carboxylate-based MOFs. However, in many studies, Ce^{4+} has been found to be a more vital Lewis acid. The 4f orbital of Ce also exhibits stronger interaction with the P=O bond, thereby increasing the reaction rate. Due to the instability of Ce-based MOFs, investing in Zr/Ce-based MOFs could be a lucrative field. The molar ratios of incorporated Ce and Zr in mixed-metal MOFs are as follows: U01 (1Ce : 5Zr), U02 (2Ce : 4Zr), U03 (3Ce : 3Zr), D01 (2Ce : 4Zr), D02 (5Ce : 1Zr), M01 (0.5Ce : 5.5Zr), M02 (2Ce : 4Zr), and M03 (5Ce : 1Zr). In all the cases above, an increase in the Ce/Zr molar ratio resulted in an extended unit cell, which was logical due to the higher atomic radius of Ce. TGA reports have shown that the U series (U01, U02, U03) exhibited structural defects and a decrease in collapse temperature. N_2 absorption showed type I behavior, confirming their microporous nature. BET analysis revealed a decrease in surface area for the D series to 825 $m^2\ g^{-1}$ according to Jacobson *et al.* **MOF-808** with the **reo** topology provided better access for Ce substitution, a property that **UiO-66** did not possess. Therefore, M01 and M02 exhibited higher BET surface areas, while M03 showed a lower surface area compared to MOF-808, likely due to its lower thermal stability.

In the second stage, the doping of magnesium was studied, which was first reported by Gil-San-Milan *et al.* They used $[Mg(OMe)_2(MeOH)_2]_4$ for the metalation of the same MOFs. They reported that **UiO-66** with **ftw** topology did not show any changes because Mg could not infiltrate into the micropores. However, in **NU-1000** and **MOF-808**, Mg was added to the clusters, resulting in $MgZr_5(OH)_6$. Comparing **MOF-808** and **NU-1000**, **MOF-808** exhibited better catalytic ability, indicating that since metalation only occurred in meso-sized pores, while nerve agent diffusion occurred in both meso and micro pores, the **spn** topology with unmixed pores showed better performance in nerve agent removal.

Garevand *et al.* reported merging Ce and Zr has an excellent effect on nerve agent removal, and also doping Mg in the system increases its catalytic performance.[79,137] Nguyen *et al.* reported **reo**-net MOF termed **Reo-MOF-1**, synthesized with solvothermal method, using 4-sulfonaphthalene-2,6-dicarboxylate ($HSNDC^{2-}$) as linkers and $Zr_6O_8(H_2O)_8(CO_2)_8$ for clusters. they reported this MOF has **reo** structure with 23 Å central cages. As we expect from reo topology this MOF is also have eight 9 Å corner-shared octahedral cages too. The structure observed in **reo-MOF-1**, resembling that found in **DUT-52** (**fcu** topology), is distinguished by the absence of body-centered packing of the 12-connected $Zr_6O_4(OH)_4(CO_2)_{12}$ clusters. This absence is

attributed to the subtle but crucial influence exerted by the bulkiness of functional groups on the linkers. The finding is supported by control experiments in which the ratio of H_3SNDC/naphthalene-2,6-dicarboxylate linkers was varied. It is affirmed that bulky functionalities play a pivotal role in defect-controlled synthesis. The **reo-MOF-1$_A$** framework was obtained through linker exchange, resulting in a chemically and thermally stable material, despite its large pores. Remarkably, permanent porosity is exhibited by **reo-MOF-1$_A$** (with BET and Langmuir SA values of 2104 $m^2\ g^{-1}$ and 2203 $m^2\ g^{-1}$, respectively). Due to these remarkable structural features, a significant enhancement in the yield of Brønsted acid-catalyzed reactions is achieved by **reo-MOF-1A**. Upon analyzing the diffraction data of the as-synthesized **reo-MOF-1** material, it is determined that the framework adopts a crystalline structure in the cubic space group $Pm\bar{3}$ (no. 200), with a unit cell length measuring 23.6938 Å. This suggests that the Zr clusters within **reo-MOF-1** are connected by $SNDC^{3-}$/$HSNDC^{2-}$ linkers, mirroring the arrangement observed in **DUT-52**. Notably, the absence of 12-connected $Zr_6O_4(OH)_4(CO_2)_{12}$ clusters at the body-centered position in **DUT-52** is confirmed in **reo-MOF-1**, as evidenced by the presence of reflections that would be forbidden in a body-centered unit cell. To refine the atomic positions within the lattice, a comprehensive Rietveld refinement is carried out on the proposed structure, resulting in successful refinement and low *R*-values. In their report they also mentioned high thermal stability and high BET surface area.[138] Same research group in another paper used this MOF for ultra-high removal of cationic malachite green dye from water. Topology of this product modified for this application as there is nearly 1 nm side cages which can absorb and stabilized dye in themselves. In their study, they investigated influence of pH and material content. They proposed, duo to SO_3H groups which is present in **reo-MOF-1** structure mechanism for adsorption, the adsorption mechanism of MG can be analyzed by examining various interactions, such as electrostatic forces and π–π interactions.[139] As observed, the connectivity of this topology differs from that of the **csq** topology. The nodes are connected in a (4,6)-fashion, resulting in a uniform, non-hierarchical, and three-dimensional network. The **reo** topology typically forms a three-dimensional structure that resembles a zeolitic network with symmetrical features. In the **reo** topology, the pores are generally smaller and more uniform. Structures with the **reo** topology are typically stable and resistant to temperature fluctuations and chemical conditions.

2.8 the topology

the is one of the topologies that is suitable for PSM because in this topology, there are large sodalite-shaped cages that are surrounded by 12 channels. They are excellent for the penetration of guest molecules. **NU-1200** is the first Zr-MOF designed with **the** topology and obtained by controlling the geometry of its constituent units. With 8 and 6 junction structures (in **csp**, **bcu**, and **spn** topologies), several coordination sites are covered with labial OH or H_2O ligands and are suitable for substitution reactions or site limiting. The goal is to create some spatial constraints on the linker to create a triangular prism to reach **the** topology. This highly penetrating topology shows that Zr clusters are readily available for easy PSM execution. The ligand used is TMTB, which caused the carboxylates in this ligand to lock perpendicular in the benzoic plate. Although the structure remains D_3h, but ligands are not in the same plane. For PSM: metal must react with OH^- and H_2O, the metal precursor must be solved by solvent but this solvent must not be coordinated, the acid from the modulator removal should not damage the MOF structure, and the ligand attached to the modulator causes rotation, destruction, and defect in the cluster.[66]

Chen *et al.* documented a robust heterogeneous molybdenum catalyst, constituted by –OH/H_2O metal grafting sites situated on the Zr_6 cluster of the mesoporous MOF **NU-1200**. This MOF possesses a mesoporous configuration, with terminal hydroxyl groups present on the Zr_6 cluster. **The** Zr-MOFs are comprised of 8-connected $[Zr_6(\mu_3\text{-}O)_4(\mu_3\text{-}OH)_4]^{12+}$ clusters and three-topic 4,4′,4″-(2,4,6-trimethylbenzene-1,3,5-triyl)-tribenzoic acid (TMTB) linkers, and they adopt a specific topology as illustrated in Fig. 16. The structure showcases 1.4 nm sodalite-like cages and

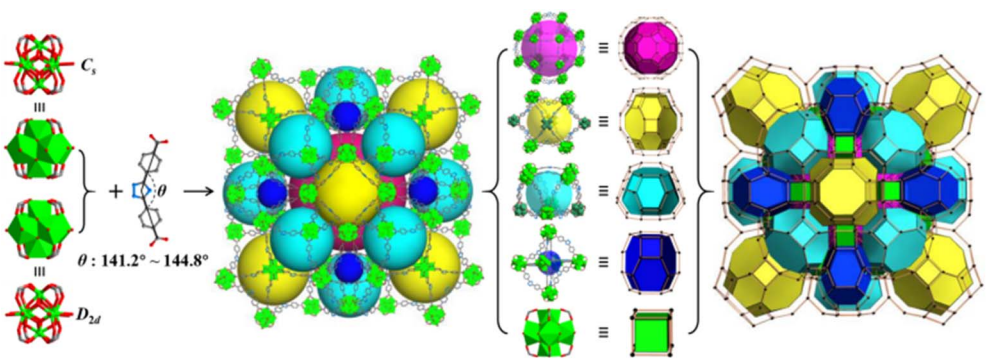

Fig. 17 Diagrammatic illustration of Zr-TZDB-**bon**-MOF: in the first column, zirconium-based inorganic MBBs with two C_s and D_2d symmetry group are accompanied by a bent organic linker (θ, 141.2–144.8°) TZDB. Second column showing formation of 3D MOF with four different cages which magnified in the third column with pink color that showed rhombicuboctahedral, yellow color that showed cuboctahedral, aquamarine showed square antiprismatic and blue which represents octahedral cages. Resulting in the augmented **bon** natural tiling. Zr = green, C = gray, N = blue, and O = red. Hydrogen atoms are hidden for simplicity.[141] From ref. 140 with permission. Copyright 2020, Elsevier.

additional interwoven mesoporous 2.2 nm channels, classified as mesopores. Given that each cluster is linked to eight linkers, a total of four unsaturated terminals with hydroxyl/aqua (–OH/H_2O) groups are available, acting as grafting sites for active metal ions. These metal ions can be introduced through Solvothermal deposition In Metal–organic frameworks (SIM), a post-synthetic technique. In comparison to other 8-connected MOFs like **NU-1000** and **NU-1008**, which demonstrate the **csq** topology and a characteristic c-pore, **NU-1200** uniquely allows the anchoring of metal active species exclusively at the –OH/H_2O groups located in the mesopores. Additionally, the layered structure of **NU-1200** enhances the diffusion of substrates, rendering it a promising heterogeneous base with the potential to provide consistently distributed active sites within its confined pore spaces.[140]

2.9 bon topology

Two isometric Zr-based metal–organic frameworks (MOFs) with **bon** and **reo** topologies were synthesized solvothermally using $ZrCl_4$ and a bent ditopic carboxylate ligand. These MOFs are characterized by their mesoporous nature and exceptional stability. In contrast to the largest cage in **MIL-101**, the MOF which has **bon** topology consists of 24 metal clusters, equivalent to 144 zirconium atoms (as opposed to 126 in chromium), and 48 TZDB groups, which are novel in the context of MOFs. Cage which configured as **rco** shaped features twenty rectangular (approximately 10.8 × 20.2 × 2 Å), six square (approximately 15.5 Å), and eight triangular (approximately 8.8 Å) windows. This cage is encased by 12 **sap**, eight **oct**, and six **cuo** cages. By viewing the Metal Building Blocks (MBBs) as eight-connected quadrangular prismatic Secondary Building Units (SBUs), the **ZrTZDB-bon-MOF** can be described as a single-node net with a bon topology (refer to Fig. 17).

Single Crystal X-ray Diffraction (SCXRD) analysis highlights the distinctions between **Zr-TZDB-reo-MOF** and **Zr-TZDB-bon-MOF** in terms of unit cell parameters and space groups. **Zr-TZDB-reo-MOF** is composed of a crystallographically independent half TZDB linker and two zirconium ions. The reo topology involves a combination of two Zr_1 and four Zr_2 ions with eight μ_3-OH/O, eight terminal –OH/H_2O groups, and eight distinct carboxylate groups, resulting in an identical MBB of $[Zr_6O_4(OH)_8(H_2O)_4(O_2C^-)_8]$, albeit with D_{2h} symmetry (see Fig. 18). **Zr-TZDB-reo-MOF** is surrounded by cuo and oct cages with diameters of 25.3 Å and 20.2 Å, respectively.[141]

2.10 hbr topology

Darche *et al.* showed a modulator-based synthesis for a MOF named **DUT-126** with $Zr_6O_4(OH)_4$ cluster and H_2TDC as a linker and trifluoroacetic acid as a modulator to produce **hbr** topology with (8,8)-connected SBU. Although the linker and cluster of **DUT-126** and **DUT-68** were completely the same, but their topology was different mainly because of the linkers place. This was the first **hbr** topology reported. **hbr** presents two kinds of micropores (0.58 nm) and middle-sized pores (1.18 nm) and one hexagonal meso channel (2.28 nm). The compound is stable in water and shows permanent porosity if activated from DMF in vacuum at temperatures lower than 180 °C. They reported BET surface area of 1297 $m^2\ g^{-1}$ and 0.48 $cm^3\ g^{-1}$ for total pore volume. Since the reduced connectivity of these MOF, functional groups could connect directly to metal clusters, and this property improves the catalytic capability of the system.[75]

2.11 Other topologies

Recently a new MOF called **CAU-45** was reported by Leubner *et al.* This MOF has 6 and 12 metal nuclear ($[Zr_6(\mu_3\text{-}O)_4(\mu_3\text{-}OH)_4]^{12+}$ and $[Zr_{12}(\mu_3\text{-}O)_8(\mu_3\text{-}OH)_8(\mu\text{-}OH)_6]^{18+}$) and 5-acetamido-isophthalic acid as ligand. Also Garai *et al.* reported another 6 and 12 connected nods in MOF, **MIP-206** that also synthesized with isophthalic acid and showed same 3-dimensional structure. They showed formic-acid-based chemical hydrogen storage when Pd-nano particles doped in MOF structure.[84] **CAU-45** exhibits a honeycomb structure with the $[Zr_{30}O_{20}(OH)_{26}(OAc)_{18}L_{18}]$ formula. Leubner *et al.* reported zirconium acetate 5-acetamido isophthalic acid and acetic acid in a solvothermal reaction in two days achieved **CAU-45** rode type crystals with the

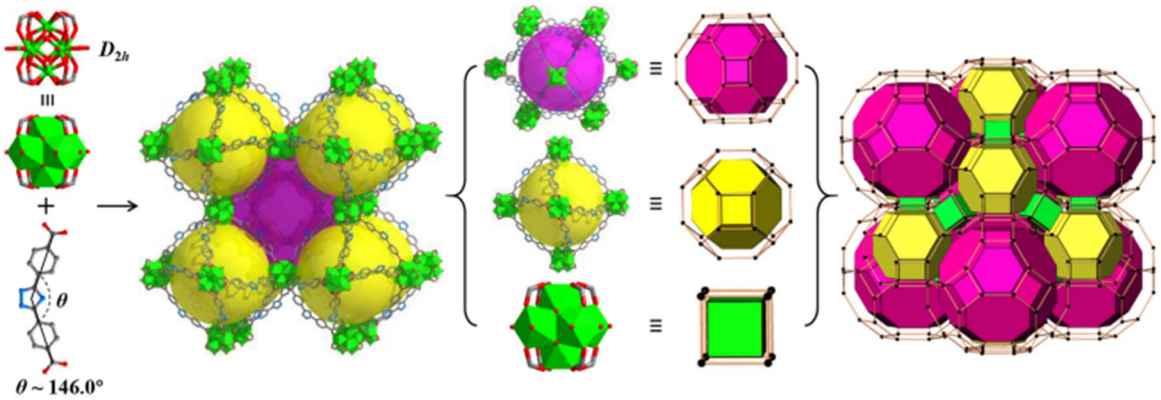

Fig. 18 Schematic representation of Zr-TZDB-**reo**-MOF: first column, zirconium-based hexanuclear inorganic MBB with D_{2h} symmetry group and bent organic linker ($\theta \sim 146.0°$) TZDB. Second column showing 3D MOF with two different cages which magnified in the third column with pink color for cuboctahedral and yellow which represented octahedral cages. Leading to the enhanced **reo** natural tiling. Zr is represented in green, C in gray, N in blue, and O in red. Hydrogen atoms are hidden for simplicity.[141] From ref. 140 with permission. Copyright 2020, Elsevier.

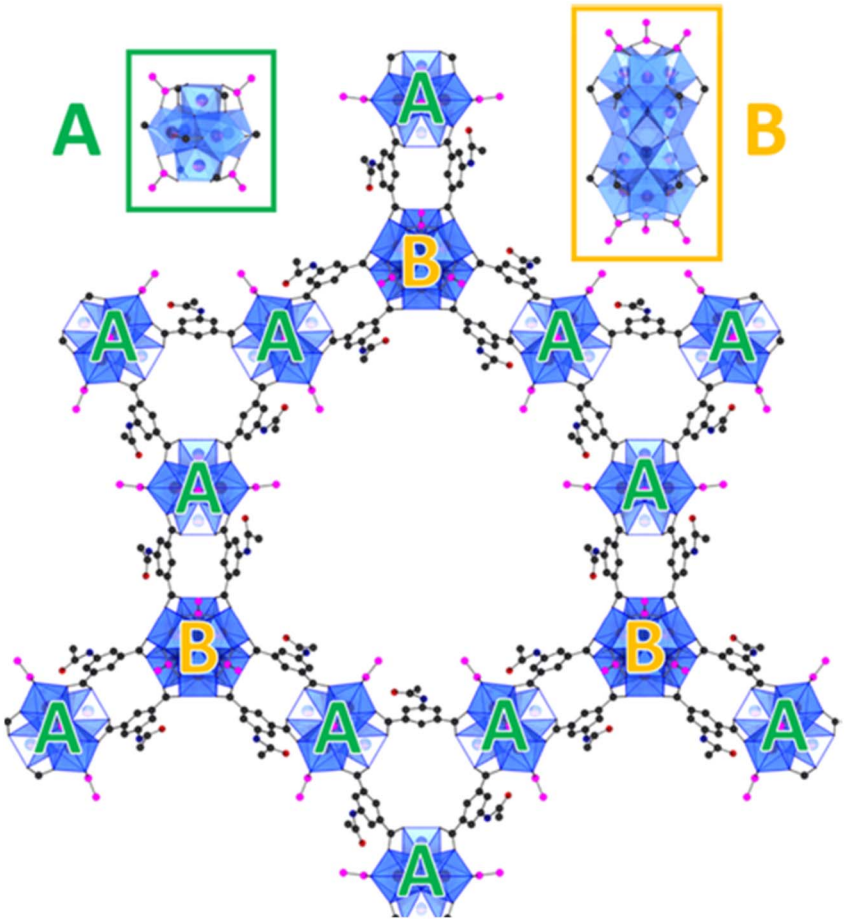

Fig. 19 Secondary building units (SBUs) of **CAU-45** and their connection to a layer motif through 5-acetamido isophthalate ions. (A) Hexanuclear clusters. (B) Dodecanuclear clusters. Carbon atoms from the linker are shown in black, and acetate carbon atoms are in pink. Zirconium is depicted in bronze, oxygen in red, nitrogen in dark blue, and hydrogen is not displayed. Zirconium–oxygen clusters are highlighted in blue.[54] From ref. 54 with permission. Copyright 2020, American Chemical Society.

size of 0.3 to 3 μm. Stok *et al.* also reported a method that achieved low crystallized structure by using cRED crystal structure and unit cell determined. **CAU-45** crystallizes in the hexagonal space group $P6_3/mmc$ with $a = 33.802(4)$ and $c = 29.096(5)$ Å, and the *c*-axis is arranged along the rod. This MOF has two different clusters, which is the first hexa- and dodecanuclear cluster reported. Before this, Zhang *et al.* reported a MOF with Zr_8 and Zr_6 clusters. The hexanuclear clusters show a presence of four acetate ligands per cluster, and in contrast, the dodecanuclear clusters display six acetate ligands per cluster. Each Zr_{12} combined two other Zr_{12} and make a thrimer connected by three linkers. Each unit-cell contains two trimers and two other free clusters. The description of the structure below assumes the inclusion of hydrogen atoms and hydrogen bonds that helps the layered structure of MOF gather together to be reinforced (Fig. 19).[54]

The synthesis of various MOFs with different topologies from the same materials was not an unprecedented research topic. Zhou *et al.* reported that by modifying the H_4TPCB ligand at other sites, different topologies could be achieved. Additionally, numerous reports have documented the creation of different MOFs with distinct topologies and connectivity using the same Zr_6 cluster and H_4TCPP ligand.[142]

Chen *et al.* reported a significant study that showed how we could control topology by changing solvent or modulator. They used spatially restrained ligand H_4TCPB-Br_2 and Zr_6 clusters and achieved 4 completely anti-phase MOFs. Using DEF as the solvent and formic acid as modulator, they achieved to **NU-500** a novel MOF with extremely new (4,4,4,5) connected topology and $[Zr_6(\mu\text{-}O)_4(\mu\text{-}OH)_4(HCOO)_4(OH)_{3.5}(H_2O)_{3.5}(TCPB\text{-}Br_2)(H_2\text{-}TCPBBr_2)_{0.25}]$ formula that was unprecedented. They reported that **NU-500** has block-shaped monoclinic crystals with 9×10 Å foursquare pores in a microspore fashion. They also reported only under tightly controlled conditions, **NU-500** was formed, and is a kinetic driven product in the synthetic pathway of **NU-600** and **NU-1008**.

NU-600 with **she** topology and $[Zr_6(\mu\text{-}O)_4(\mu\text{-}OH)_4(CH_3\text{-}COO)_6(TCPB\text{-}Br_2)_{1.5}]$ formula formed using acetic acid as modulator and DEF as a solvent. It has 3 types of channels; 13 and 19 Å cubic channels along the *z*-axis and another tetragonal channel with size of 13×19 Å^2, this one along the *x*-axis. **NU-906** crystals were oval-shaped with **scu** topology and $[Zr_6(\mu$-

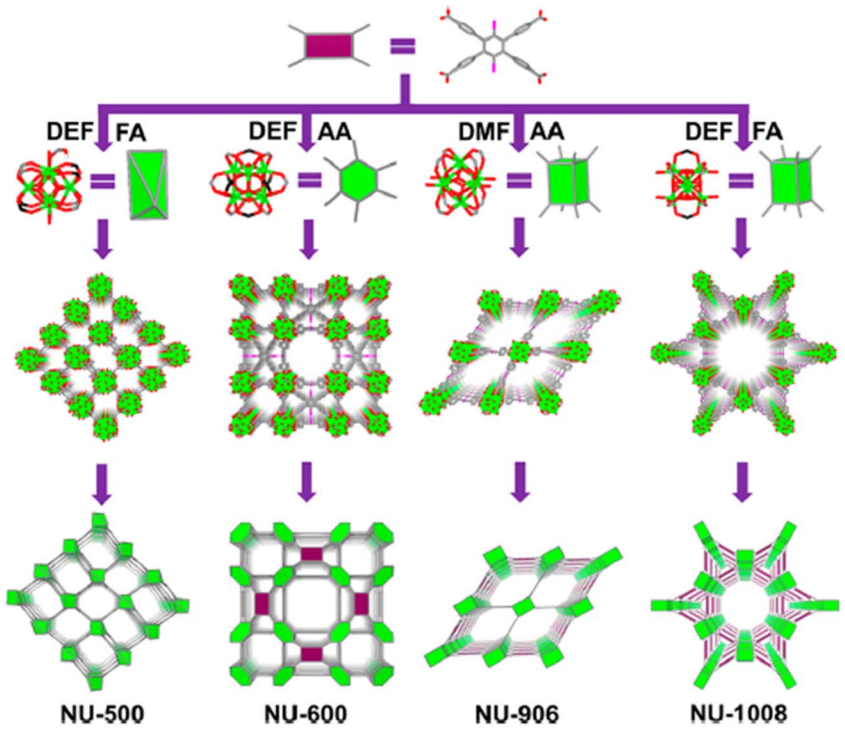

Fig. 20 This figure shows how the use of the same raw materials but different solvents and modulators can create different topologies in the product. Color scheme: C, gray; O, red; Br, pink; Zr, green. H atoms in the structures are omitted for clarity. Acetic acid is termed as AA and formic acid is termed as FA.[6] From ref. 7 with permission. Copyright 2020, American Chemical Society.

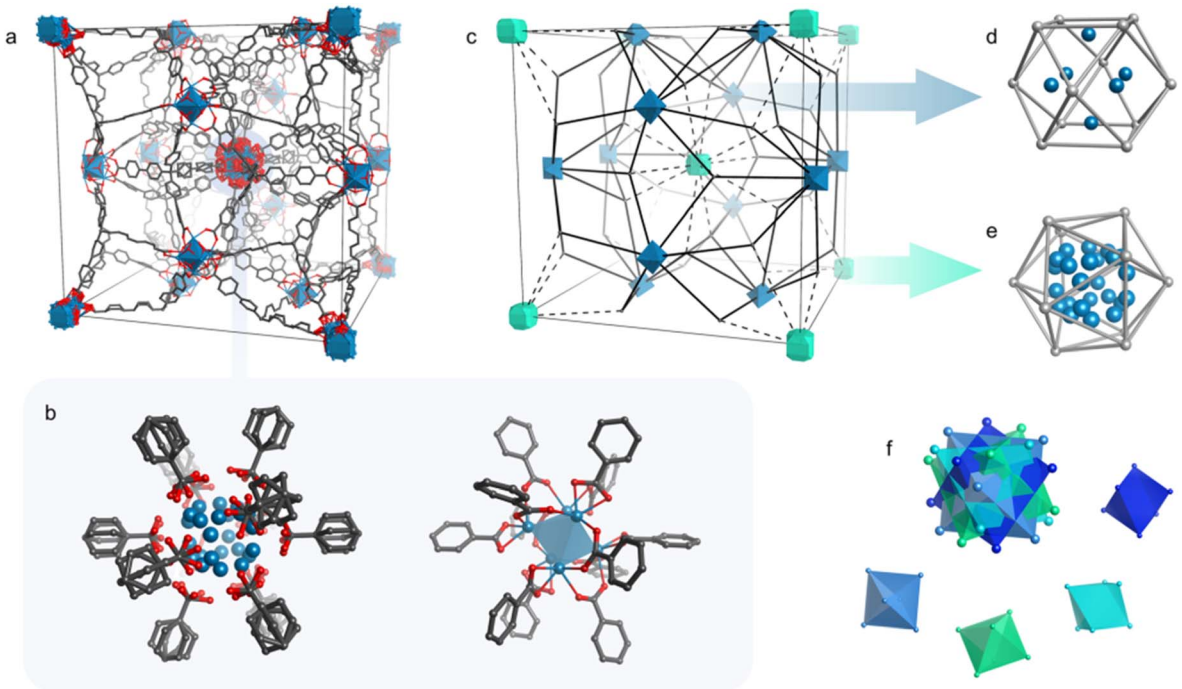

Fig. 21 The crystal structure of c-(4,12)MTBC-Zr_6 is presented, depicting the complete unit cell (a) and emphasizing the modeled average disordered cluster site alongside one of its four potential local variants (b). The topological view (c) is provided, and the simplified representation of the ordered and disordered cluster sites (d) and (e) distinguishes Zr atoms in blue and the surrounding linker carboxylate carbons in silver. The superimposition of four Zr6 octahedra in the disordered cluster is highlighted by differentiating octahedra with various colors (f). For clarity, only the fraction of linkers within the unit cell is shown.[82] From ref. 82 with permission. Copyright 2023, American Chemical Society.

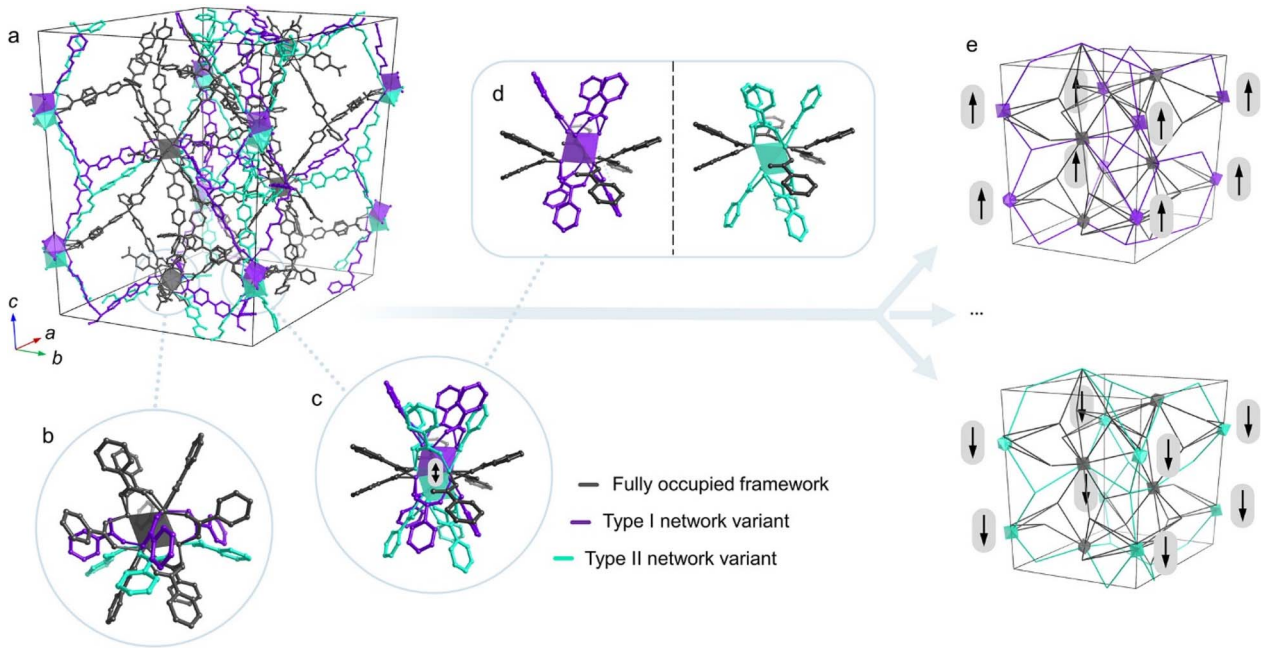

Fig. 22 Attributes of the intricate topology within the tr-(4,12)MTBC-Zr6 structure are outlined. The complete unit cell (a) is depicted, showcasing fully occupied clusters and linkers in gray (b), along with alternative framework fractions in violet and turquoise. Clusters positioned on the edges of the unit cell exhibit disorder in two alternative positions (c), either above or below the (1/4 0 0) site (d). The structures resulting from all "upshifted" or all "downshifted" clusters among all possible periodic or aperiodic networks are presented (e).[82] From ref. 82 with permission. Copyright 2020, American Chemical Society.

$O)_4(\mu\text{-}OH)_4(OH)_4(TCPB\text{-}Br_2)_2]$ were manufactured using DMF solvent and acetic acid as the modulator. All channels are similarly 12 × 27 Å and rhombic. Also, **NU-1008** was synthesized using DMF as the solvent and formic acid as modulators and showed a familiar **csq** topology with 13 Å triangular channels and 30 Å hexagonal ones. Absorption behaviors of these MOFs were also investigated. Since there is no difference in materials, it could quickly understand that their different absorption behavior came from their different topology and spatial position of ligands. **NU-500**, **NU-600**, **NU-906**, and **NU-1008** absorb *n*-hexane of 5.2 $cm^3\ g^{-1}$, 103.5 $cm^3\ g^{-1}$, 79,7 $cm^3\ g^{-1}$, and 167.7 $cm^3\ g^{-1}$ respectively. They also studied the absorption of CEES and reported that **NU-906**, despite its smaller pores, showed higher absorption that is comes from higher interactions between ligands and CEES obtained for the special unique position of ligands (Fig. 20).[6]

In Lotsch study, the simultaneous synthesis of three distinct MOFs is documented, utilizing the same $Zr_6O_4(OH)_4$ clusters and methanetetrakis(*p*-biphenyl-carboxylate) (MTBC) linkers. Two novel structural models are introduced based on single-crystal diffraction analysis, specifically, cubic c-(4,12)MTBC-M_6 and trigonal tr-(4,12)MTBC-M_6, encompassing 12-coordinated clusters and 4-coordinated tetrahedral linkers. Significantly, the cubic phase showcases a new architecture relying on orientational cluster disorder, crucial for its formation, and has been examined through a combination of average structure refinements and diffuse scattering analysis from both powder and single-crystal X-ray diffraction data. They believe varying of topology of Zr-based MOF are related to combinations of linkers and clusters and limited by these factors. Enhancing the range of topologies in MOFs can be achieved by utilizing linker flexibility, which helps alleviate moderate geometric frustration in the structure. But on the other hand, ideal geometry of the building blocks limited this promised diversity. For c-(4,12) MTBC-Zr_6 they used benzoic acid as modulator to gain 2–5 μm truncated octahedra crystals. This structure only had $Zr_6O_4(OH)_4$ SBUs. They detailed structure and place of SBUs to define this new topology. Fig. 21 schematically illustrate place of SBUs in crystal.

It was mentioned that synthesis of c-(4,12)MTBC-Zr_6 does not results in pure phase. They report two another phase of this structure. The initial discovery was made through single-crystal X-ray diffraction (SCXRD), identifying the tetragonal MOF **PCN-521** (4,8)-**flu** (which was previously reported by Zhang *et al.*[143]). The subsequent finding unveiled a previously unreported MTBC-Zr_6 framework with identical (4,12)MTBC-Zr_6 connectivity, albeit possessing a trigonal symmetry. called tr-(4,12) MTBC-Zr_6.82 Structural detail of this new topology is discussed in Fig. 22.

3. Conclusions and outlook

Topology plays a central role in defining the chemical and physical properties of metal–organic frameworks (MOFs), directly influencing their pore size, stability and potential applications. Topologies with higher connectivity often result in smaller pore sizes and grater thermal and mechanical stability, making them advantageous for applications under harsh

conditions. In contrast, the use of larger organic linkers can lead to frameworks with lower connectivity and larger mesopores, which are essential for applications requiring the diffusion of bulky molecules. This review investigates 10 famous topologies csq, scu, spn, the, she, ftw, reo, flu, hbr, alb and also some other and non-repetitive structures. We not only indicate which specific structures arise from each topology, but also highlighted the key properties of this frameworks. The review is an application-oriented review and as much as possible we have tried to mention all the applications that were reviewed for each framework and mention their strengths and weaknesses. We showed that the choice of structure can really help optimize a framework in an application. This review has shown how channel-based topologies (such as csq or ftw) are particularly suited for catalysis or sequential guest uptake, such as enzyme cascade systems, due to their directional pore architecture. On the other hand, cage-based topologies (such as flu or spn) offer isolated cavities ideals for drug encapsulation and controlled release. We also shown that how choosing wrong topologies for a project can reduced optimization in a project. The result of this review specifies achieving the best results in a scientific project is only possible with sufficient knowledge of the structure of the chemical we are dealing with. Although a project can be completed by choosing the wrong chemical structure, understanding the structures and their properties can save a research group money, time, and resources. We have also highlighted synthetic approaches and design principles that allow researchers to tailor topology through the choice of linkers, modulators and synthetic conditions. These two issues make our review a comprehensive resource for understanding, learning, and applying different topologies with an understanding of the advantages and disadvantages of these structures.

Author contributions

All authors of this manuscript contributed equally to the process of ideation, research and data collection, and writing the final manuscript.

Conflicts of interest

The authors declare no conflict of interest.

Data availability

No primary research results, software or code have been included and no new data were generated or analyzed as part of this review.

Acknowledgements

The authors would like to acknowledge the financial support of University of Tehran for this research under grant number 01/1/389845.

References

1 S. Sonal and B. K. Mishra, *Chem. Eng. J.*, 2021, **424**, 130509.
2 J. Zhang, A. R. Oganov, X. Li, M. Mahdi Davari Esfahani and H. Dong, *J. Appl. Phys.*, 2017, **121**, 15.
3 K. Gurushantha, K. Anantharaju, H. Nagabhushana, S. Sharma, Y. Vidya, C. Shivakumara, H. Nagaswarupa, S. Prashantha and M. Anilkumar, *J. Mol. Catal. A: Chem.*, 2015, **397**, 36–47.
4 L. Renuka, K. Anantharaju, S. Sharma, H. Nagaswarupa, S. Prashantha, H. Nagabhushana and Y. Vidya, *J. Alloys Compd.*, 2016, **672**, 609–622.
5 Z. Wang, M. Xing, W. Fang and D. Wu, *Appl. Surf. Sci.*, 2016, **366**, 67–77.
6 Y. Chen, X. Zhang, M. R. Mian, F. A. Son, K. Zhang, R. Cao, Z. Chen, S.-J. Lee, K. B. Idrees and T. A. Goetjen, *J. Am. Chem. Soc.*, 2020, **142**, 21428–21438.
7 S. Soltani, K. Akhbari and J. White, *CrystEngComm*, 2021, **23**, 7450–7461.
8 H. Choi, A. W. Peters, H. Noh, L. C. Gallington, A. E. Platero-Prats, M. R. DeStefano, M. Rimoldi, S. Goswami, K. W. Chapman and O. K. Farha, *ACS Appl. Energy Mater.*, 2019, **2**, 8695–8700.
9 Y. Noori and K. Akhbari, *RSC Adv.*, 2017, **7**, 1782–1808.
10 T. Minh Nguyet Bui, T. Ky Vo, N. Hoang Yen Phuong, V. Hung Nguyen, V. Cuong Nguyen, Q. Hung Nguyen and N. Thi Thanh Dang, *Sep. Purif. Technol.*, 2025, **355**, 129723.
11 P. Kumar, A. Deep and K.-H. Kim, *TrAC, Trends Anal. Chem.*, 2015, **73**, 39–53.
12 W. Cheng, X. Tang, Y. Zhang, D. Wu and W. Yang, *Trends Food Sci. Technol.*, 2021, **112**, 268–282.
13 P. G. Oorimi, A. Tarlani, R. Zadmard and J. Muzart, *Microchem. J.*, 2023, **189**, 108494.
14 R. J. Drout, L. Robison and O. K. Farha, *Coord. Chem. Rev.*, 2019, **381**, 151–160.
15 S. Mao, X. Cheng, Z. Zhu, Y. Chen, C. Li, M. Zhu, X. Liu, F. Lu and H.-M. Qin, *Enzyme Microb. Technol.*, 2020, **132**, 109441.
16 S. S. Nadar and V. K. Rathod, *Int. J. Biol. Macromol.*, 2018, **120**, 2293–2302.
17 L. Yang, X. Zeng, W. Wang and D. Cao, *Adv. Funct. Mater.*, 2018, **28**, 1704537.
18 M. Parsaei, K. Akhbari and S. Kawata, *Cryst. Growth Des.*, 2023, **23**, 5705–5718.
19 S. Salimi, K. Akhbari, S. M. F. Farnia and J. M. White, *Cryst. Growth Des.*, 2022, **22**, 1654–1664.
20 K. Akhbari and A. Morsali, *Dalton Trans.*, 2013, **42**, 4786–4789.
21 B. Forouzesh Rad, H. Mahdavi, M. Forouzesh Rad and M. Baghdadi, *J. Polym. Environ.*, 2022, **30**, 3875–3889.
22 H. K. Okoro, S. O. Ayika, J. C. Ngila and A. C. Tella, *Appl. Water Sci.*, 2018, **8**, 1–10.
23 M. Rahmani, A. Abbasi and M.-S. Hosseini, *J. Photochem. Photobiol., A*, 2023, **445**, 115019.
24 R. K. Alavijeh, K. Akhbari and J. White, *Cryst. Growth Des.*, 2019, **19**, 7290–7297.

25 G. Sriram, A. Bendre, E. Mariappan, T. Altalhi, M. Kigga, Y. C. Ching, H.-Y. Jung, B. Bhaduri and M. Kurkuri, *Sustainable Mater. Technol.*, 2022, **31**, e00378.
26 Y. Pan, K. Sun, S. Liu, X. Cao, K. Wu, W.-C. Cheong, Z. Chen, Y. Wang, Y. Li and Y. Liu, *J. Am. Chem. Soc.*, 2018, **140**, 2610–2618.
27 M. Nakhaei, K. Akhbari and A. Davoodi, *CrystEngComm*, 2021, **23**, 8538–8545.
28 R. K. Alavijeh, S. Beheshti, K. Akhbari and A. Morsali, *Polyhedron*, 2018, **156**, 257–278.
29 S. Soltani and K. Akhbari, *New J. Chem.*, 2022, **46**, 19432–19441.
30 S. Soltani and K. Akhbari, *CrystEngComm*, 2022, **24**, 1934–1941.
31 R. K. Alavijeh and K. Akhbari, *Colloids Surf., B*, 2022, **212**, 112340.
32 M. Parsaei and K. Akhbari, *Inorg. Chem.*, 2022, **61**, 19354–19368.
33 M. Parsaei and K. Akhbari, *Inorg. Chem.*, 2022, **61**, 5912–5925.
34 R. Karimi Alavijeh and K. Akhbari, *Inorg. Chem.*, 2020, **59**, 3570–3578.
35 R. Karimi Alavijeh and K. Akhbari, *ChemBioChem*, 2023, **24**(20), e202300415.
36 M. Alvaro, E. Carbonell, B. Ferrer, F. X. Llabrés i Xamena and H. Garcia, *Chem.–Eur. J.*, 2007, **13**, 5106–5112.
37 Y. Ban, N. Cao and W. Yang, *Research*, 2020, 2020.
38 M. Li, C. Ma, X. Liu, J. Su, X. Cui and Y. He, *Chem. Sci.*, 2018, **9**, 5912–5918.
39 B. Chen, C. Liang, J. Yang, D. S. Contreras, Y. L. Clancy, E. B. Lobkovsky, O. M. Yaghi and S. Dai, *Angew. Chem., Int. Ed.*, 2006, **45**, 1390–1393.
40 M. Parsaei, K. Akhbari and J. White, *Inorg. Chem.*, 2022, **61**, 3893–3902.
41 M. Parsaei, K. Akhbari, E. Tylianakis, G. E. Froudakis, J. M. White and S. Kawata, *Cryst. Growth Des.*, 2022, **22**, 7221–7233.
42 R. Karimi Alavijeh, K. Akhbari, M. C. Bernini, A. s. A. García Blanco and J. M. White, *Cryst. Growth Des.*, 2022, **22**, 3154–3162.
43 J. Shui, C. Chen, L. Grabstanowicz, D. Zhao and D.-J. Liu, *Proc. Natl. Acad. Sci. U. S. A.*, 2015, **112**, 10629–10634.
44 R. G. Pearson, *J. Chem. Educ.*, 1968, **45**, 581.
45 S. Yuan, L. Feng, K. Wang, J. Pang, M. Bosch, C. Lollar, Y. Sun, J. Qin, X. Yang and P. Zhang, *Adv. Mater.*, 2018, **30**, 1704303.
46 J. H. Cavka, S. Jakobsen, U. Olsbye, N. Guillou, C. Lamberti, S. Bordiga and K. P. Lillerud, *J. Am. Chem. Soc.*, 2008, **130**, 13850–13851.
47 T. Si, L. Wang, X. Lu, X. Liang, S. Wang and Y. Guo, *Analyst*, 2020, **145**, 3851–3856.
48 Y. Chi and P.-T. Chou, *Chem. Soc. Rev.*, 2010, **39**, 638–655.
49 D. Liu, D. Zou, H. Zhu and J. Zhang, *Small*, 2018, **14**, 1801454.
50 F. E. Chen, T. A. Pitt, D. J. Okong'o, L. G. Wetherbee, J. J. Fuentes-Rivera and P. J. Milner, *Chem. Mater.*, 2022, **34**, 3383–3394.
51 H.-Y. Guan, R. J. LeBlanc, S.-Y. Xie and Y. Yue, *Coord. Chem. Rev.*, 2018, **369**, 76–90.
52 M. K. Albolkany, C. Liu, Y. Wang, C. H. Chen, C. Zhu, X. Chen and B. Liu, *Angew. Chem., Int. Ed.*, 2021, **60**, 14601–14608.
53 C. Koschnick, R. Stäglich, T. Scholz, M. W. Terban, A. von Mankowski, G. Savasci, F. Binder, A. Schökel, M. Etter and J. Nuss, *Nat. Commun.*, 2021, **12**, 3099.
54 S. Leubner, V. E. Bengtsson, K. Synnatschke, J. Gosch, A. Koch, H. Reinsch, H. Xu, C. Backes, X. Zou and N. Stock, *J. Am. Chem. Soc.*, 2020, **142**, 15995–16000.
55 Y. Bai, Y. Dou, L.-H. Xie, W. Rutledge, J.-R. Li and H.-C. Zhou, *Chem. Soc. Rev.*, 2016, **45**, 2327–2367.
56 D. N. Dybtsev, A. A. Sapianik and V. P. Fedin, *Mendeleev Commun.*, 2017, **27**, 321–331.
57 R. J. Drout, L. Robison, Z. Chen, T. Islamoglu and O. K. Farha, *Trends Chem.*, 2019, **1**, 304–317.
58 H. Xiao and S. Liu, *Mater. Des.*, 2018, **155**, 19–35.
59 H. Zhang, P. Xiong, G. Li, C. Liao and G. Jiang, *TrAC, Trends Anal. Chem.*, 2020, **131**, 116015.
60 A. Davoodi, K. Akhbari and M. Alirezvani, *CrystEngComm*, 2023, 3931–3942.
61 P. Wang, J. Feng, Y. Zhao, S. Gu and J. Liu, *RSC Adv.*, 2017, **7**, 55920–55926.
62 Z. Yue, S. Liu and Y. Liu, *RSC Adv.*, 2015, **5**, 10619–10622.
63 K. J. Lee, J. H. Lee, S. Jeoung and H. R. Moon, *Acc. Chem. Res.*, 2017, **50**, 2684–2692.
64 I. D. Brown, *Struct. Chem.*, 2002, **13**, 339–355.
65 P. Li, S.-Y. Moon, M. A. Guelta, L. Lin, D. A. Gómez-Gualdrón, R. Q. Snurr, S. P. Harvey, J. T. Hupp and O. K. Farha, *ACS Nano*, 2016, **10**, 9174–9182.
66 P. Li, Q. Chen, T. C. Wang, N. A. Vermeulen, B. L. Mehdi, A. Dohnalkova, N. D. Browning, D. Shen, R. Anderson and D. A. Gómez-Gualdrón, *Chem*, 2018, **4**, 1022–1034.
67 X. Gong, H. Noh, N. C. Gianneschi and O. K. Farha, *J. Am. Chem. Soc.*, 2019, **141**, 6146–6151.
68 M. C. de Koning, M. van Grol and T. Breijaert, *Inorg. Chem.*, 2017, **56**, 11804–11809.
69 T. F. Liu, N. A. Vermeulen, A. J. Howarth, P. Li, A. A. Sarjeant, J. T. Hupp and O. K. Farha, *Eur. J. Inorg. Chem.*, 2016, **2016**, 4349–4352.
70 A. M. Bumstead, D. B. Cordes, D. M. Dawson, K. K. Chakarova, M. Y. Mihaylov, C. L. Hobday, T. Düren, K. I. Hadjiivanov, A. M. Slawin and S. E. Ashbrook, *Chem.–Eur. J.*, 2018, **24**, 6115–6126.
71 X. Gong, K. Gnanasekaran, K. Ma, C. J. Forman, X. Wang, S. Su, O. K. Farha and N. C. Gianneschi, *J. Am. Chem. Soc.*, 2022, **144**, 6674–6680.
72 X. Li, H. Wang, J. Zou and J. Li, *CrystEngComm*, 2022, **24**, 2189–2200.
73 V. Bon, V. Senkovskyy, I. Senkovska and S. Kaskel, *Chem. Commun.*, 2012, **48**, 8407–8409.
74 Z. Chen, P. Li, X. Wang, K.-i. Otake, X. Zhang, L. Robison, A. Atilgan, T. Islamoglu, M. G. Hall and G. W. Peterson, *J. Am. Chem. Soc.*, 2019, **141**, 12229–12235.
75 F. Drache, V. Bon, I. Senkovska, J. Getzschmann and S. Kaskel, *Philos. Trans. R. Soc., A*, 2017, **375**, 20160027.

76 Z. Chen, K. O. Kirlikovali, P. Li and O. K. Farha, *Acc. Chem. Res.*, 2022, **55**, 579–591.
77 B. Wang, X.-L. Lv, D. Feng, L.-H. Xie, J. Zhang, M. Li, Y. Xie, J.-R. Li and H.-C. Zhou, *J. Am. Chem. Soc.*, 2016, **138**, 6204–6216.
78 Y. Liu, J. Zou, B. Guo, Y. Ren, Z. Wang, Y. Song, Y. Yu and L. Wu, *Langmuir*, 2020, **36**, 2199–2208.
79 E. Geravand, F. Farzaneh, R. Gil-San-Millan, F. J. Carmona and J. A. Navarro, *Inorg. Chem.*, 2020, **59**, 16160–16167.
80 H. Furukawa, F. Gándara, Y.-B. Zhang, J. Jiang, W. L. Queen, M. R. Hudson and O. M. Yaghi, *J. Am. Chem. Soc.*, 2014, **136**, 4369–4381.
81 H. R. Abid, H. Tian, H.-M. Ang, M. O. Tade, C. E. Buckley and S. Wang, *Chem. Eng. J.*, 2012, **187**, 415–420.
82 C. Koschnick, M. W. Terban, R. Frison, M. Etter, F. A. Böhm, D. M. Proserpio, S. Krause, R. E. Dinnebier, S. Canossa and B. V. Lotsch, *J. Am. Chem. Soc.*, 2023, **145**, 10051–10060.
83 K. Li, S. Lin, Y. Li, Q. Zhuang and J. Gu, *Angew. Chem.*, 2018, **130**, 3497–3501.
84 M. Garai and C. T. Yavuz, *Matter*, 2021, **4**, 10–12.
85 R. Hariri, S. Dehghanpour and S. Sohrabi, *J. Inorg. Organomet. Polym. Mater.*, 2020, **30**, 4720–4731.
86 S. Pang, Y. Wu, X. Zhang, B. Li, J. Ouyang and M. Ding, *Process Biochem.*, 2016, **51**, 229–239.
87 X. Xu, S. Li, Q. Liu, Z. Liu, W. Yan, L. Zhao, W. Zhang, L. Zhang, F. Deng and H. Cong, *ACS Appl. Mater. Interfaces*, 2018, **11**, 973–981.
88 J. E. Mondloch, W. Bury, D. Fairen-Jimenez, S. Kwon, E. J. DeMarco, M. H. Weston, A. A. Sarjeant, S. T. Nguyen, P. C. Stair and R. Q. Snurr, *J. Am. Chem. Soc.*, 2013, **135**, 10294–10297.
89 Q. Zhang, J. Su, D. Feng, Z. Wei, X. Zou and H.-C. Zhou, *J. Am. Chem. Soc.*, 2015, **137**, 10064–10067.
90 J. Lyu, X. Zhang, K.-i. Otake, X. Wang, P. Li, Z. Li, Z. Chen, Y. Zhang, M. C. Wasson and Y. Yang, *Chem. Sci.*, 2019, **10**, 1186–1192.
91 S. Kato, R. J. Drout and O. K. Farha, *Cell Rep. Phys. Sci.*, 2020, **1**(1), DOI: **10.1016/j.xcrp.2019.100006**.
92 P. Deria, D. A. Gómez-Gualdrón, W. Bury, H. T. Schaef, T. C. Wang, P. K. Thallapally, A. A. Sarjeant, R. Q. Snurr, J. T. Hupp and O. K. Farha, *J. Am. Chem. Soc.*, 2015, **137**, 13183–13190.
93 X. Chen, P. Jagadesan, S. Valandro, J. T. Hupp, K. S. Schanze and S. Goswami, *ACS Mater. Lett.*, 2022, **4**, 370–377.
94 L. Xu, Y. P. Luo, L. Sun, Y. Xu, Z. S. Cai, M. Fang, R. X. Yuan and H. B. Du, *Chem.–Eur. J.*, 2016, **22**, 6268–6276.
95 J. Pang, Z. Di, J.-S. Qin, S. Yuan, C. T. Lollar, J. Li, P. Zhang, M. Wu, D. Yuan and M. Hong, *J. Am. Chem. Soc.*, 2020, **142**, 15020–15026.
96 Y. Wang, C. Hao, W. Fan, M. Fu, X. Wang, Z. Wang, L. Zhu, Y. Li, X. Lu and F. Dai, *Angew. Chem.*, 2021, **133**, 11451–11459.
97 T. He, B. Ni, X. Xu, H. Li, H. Lin, W. Yuan, J. Luo, W. Hu and X. Wang, *ACS Appl. Mater. Interfaces*, 2017, **9**, 22732–22738.
98 J. Su, S. Yuan, T. Wang, C. T. Lollar, J.-L. Zuo, J. Zhang and H.-C. Zhou, *Chem. Sci.*, 2020, **11**, 1918–1925.
99 L. Feng, Y. Wang, K. Zhang, K. Y. Wang, W. Fan, X. Wang, J. A. Powell, B. Guo, F. Dai and L. Zhang, *Angew. Chem., Int. Ed.*, 2019, **58**, 16682–16690.
100 A. Pankajakshan, M. Sinha, A. A. Ojha and S. Mandal, *ACS Omega*, 2018, **3**, 7832–7839.
101 Z. Li, A. W. Peters, V. Bernales, M. A. Ortuño, N. M. Schweitzer, M. R. DeStefano, L. C. Gallington, A. E. Platero-Prats, K. W. Chapman and C. J. Cramer, *ACS Cent. Sci.*, 2017, **3**, 31–38.
102 P. Li, S.-Y. Moon, M. A. Guelta, S. P. Harvey, J. T. Hupp and O. K. Farha, *J. Am. Chem. Soc.*, 2016, **138**, 8052–8055.
103 H. Noh, Y. Cui, A. W. Peters, D. R. Pahls, M. A. Ortuño, N. A. Vermeulen, C. J. Cramer, L. Gagliardi, J. T. Hupp and O. K. Farha, *J. Am. Chem. Soc.*, 2016, **138**, 14720–14726.
104 M. Rimoldi, J. T. Hupp and O. K. Farha, *ACS Appl. Mater. Interfaces*, 2017, **9**, 35067–35074.
105 M. F. De Lange, K. J. Verouden, T. J. Vlugt, J. Gascon and F. Kapteijn, *Chem. Rev.*, 2015, **115**, 12205–12250.
106 H. Chen, Z. Chen, O. K. Farha and R. Q. Snurr, *ACS Sustain. Chem. Eng.*, 2019, **7**, 18242–18246.
107 A. A. Talin, M. E. Foster, V. Stavila, F. L. Leonard, D. C. Spataru, M. D. Allendorf, A. C. Ford and F. El Gabaly Marquez, *Molecule@ MOF: A New Class of Electronic Materials*, Sandia National Lab (SNL-CA), Livermore, CA (United States), Sandia National, 2014.
108 T. C. Wang, I. Hod, C. O. Audu, N. A. Vermeulen, S. T. Nguyen, O. K. Farha and J. T. Hupp, *ACS Appl. Mater. Interfaces*, 2017, **9**, 12584–12591.
109 C.-W. Kung, K. Otake, C. T. Buru, S. Goswami, Y. Cui, J. T. Hupp, A. M. Spokoyny and O. K. Farha, *J. Am. Chem. Soc.*, 2018, **140**, 3871–3875.
110 C.-W. Kung, A. E. Platero-Prats, R. J. Drout, J. Kang, T. C. Wang, C. O. Audu, M. C. Hersam, K. W. Chapman, O. K. Farha and J. T. Hupp, *ACS Appl. Mater. Interfaces*, 2018, **10**, 30532–30540.
111 P. R. McGonigal, P. Deria, I. Hod, P. Z. Moghadam, A.-J. Avestro, N. E. Horwitz, I. C. Gibbs-Hall, A. K. Blackburn, D. Chen and Y. Y. Botros, *Proc. Natl. Acad. Sci. U. S. A.*, 2015, **112**, 11161–11168.
112 X. Li, K. Gao, B. Mo, J. Tang, J. Wu and H. Hou, *Inorg. Chem.*, 2021, **60**, 1352–1358.
113 D. Feng, Z. Y. Gu, J. R. Li, H. L. Jiang, Z. Wei and H. C. Zhou, *Angew. Chem.*, 2012, **124**, 10453–10456.
114 M. R. Rezaei Kahkha, S. Daliran, A. R. Oveisi, M. Kaykhaii and Z. Sepehri, *Food Anal. Methods*, 2017, **10**, 2175–2184.
115 H. Li, X. Cao, C. Zhang, Q. Yu, Z. Zhao, X. Niu, X. Sun, Y. Liu, L. Ma and Z. Li, *RSC Adv.*, 2017, **7**, 16273–16281.
116 A. Amini, M. Khajeh, A. R. Oveisi, S. Daliran, M. Ghaffari-Moghaddam and H. S. Delarami, *J. Ind. Eng. Chem.*, 2021, **93**, 322–332.
117 M. R. Ghaleno, M. Ghaffari-Moghaddam, M. Khajeh, A. R. Oveisi and M. Bohlooli, *J. Colloid Interface Sci.*, 2019, **535**, 214–226.
118 C. Bi, C. Zhang, F. Ma, X. Zhang, M. Yang, J. Nian, L. Liu, H. Dong, L. Zhu and Q. Wang, *Microporous Mesoporous Mater.*, 2021, **323**, 111223.

119 S. Nazri, M. Khajeh, A. R. Oveisi, R. Luque, E. Rodriguez-Castellon and M. Ghaffari-Moghaddam, *Sep. Purif. Technol.*, 2021, **259**, 118197.
120 X. S. Wang, M. Chrzanowski, L. Wojtas, Y. S. Chen and S. Ma, *Chem.–Eur. J.*, 2013, **19**, 3297–3301.
121 S. J. Garibay, I. Iordanov, T. Islamoglu, J. B. DeCoste and O. K. Farha, *CrystEngComm*, 2018, **20**, 7066–7070.
122 P. K. Verma, L. Huelsenbeck, A. W. Nichols, T. Islamoglu, H. Heinrich, C. W. Machan and G. Giri, *Chem. Mater.*, 2020, **32**, 10556–10565.
123 W. Morris, B. Volosskiy, S. Demir, F. Gándara, P. L. McGrier, H. Furukawa, D. Cascio, J. F. Stoddart and O. M. Yaghi, *Inorg. Chem.*, 2012, **51**, 6443–6445.
124 H.-L. Jiang, D. Feng, K. Wang, Z.-Y. Gu, Z. Wei, Y.-P. Chen and H.-C. Zhou, *J. Am. Chem. Soc.*, 2013, **135**, 13934–13938.
125 M. Lammert, H. Reinsch, C. Murray, M. Wharmby, H. Terraschke and N. Stock, *Dalton Trans.*, 2016, **45**, 18822–18826.
126 J. M. Mayers and R. W. Larsen, *Inorg. Chim. Acta*, 2021, **526**, 120537.
127 C. Tan, X. Han, Z. Li, Y. Liu and Y. Cui, *J. Am. Chem. Soc.*, 2018, **140**, 16229–16236.
128 T. K. Vo, J. Kim, J. Park, D. Q. Dao and H. B. Truong, *Chem. Eng. J.*, 2024, **481**, 148570.
129 J. B. DeCoste, J. A. Rossin and G. W. Peterson, *Chem.–Eur. J.*, 2015, **21**, 18029–18032.
130 M.-B. Kim, T.-H. Kim, T.-U. Yoon, J. H. Kang, J.-H. Kim and Y.-S. Bae, *J. Ind. Eng. Chem.*, 2020, **84**, 179–184.
131 S. Waitschat, D. Fröhlich, H. Reinsch, H. Terraschke, K. Lomachenko, C. Lamberti, H. Kummer, T. Helling, M. Baumgartner and S. Henninger, *Dalton Trans.*, 2018, **47**, 1062–1070.
132 Y.-J. Lee, Y.-J. Chang and J.-P. Hsu, *Chemosphere*, 2021, **268**, 129155.
133 D. Feng, K. Wang, J. Su, T. F. Liu, J. Park, Z. Wei, M. Bosch, A. Yakovenko, X. Zou and H. C. Zhou, *Angew. Chem., Int. Ed.*, 2015, **54**, 149–154.
134 A. M. Plonka, Q. Wang, W. O. Gordon, A. Balboa, D. Troya, W. Guo, C. H. Sharp, S. D. Senanayake, J. R. Morris and C. L. Hill, *J. Am. Chem. Soc.*, 2017, **139**, 599–602.
135 G. W. Peterson, S.-Y. Moon, G. W. Wagner, M. G. Hall, J. B. DeCoste, J. T. Hupp and O. K. Farha, *Inorg. Chem.*, 2015, **54**, 9684–9686.
136 G. Cai, P. Yan, L. Zhang, H.-C. Zhou and H.-L. Jiang, *Chem. Rev.*, 2021, **121**, 12278–12326.
137 J. E. Mondloch, M. J. Katz, W. C. Isley Iii, P. Ghosh, P. Liao, W. Bury, G. W. Wagner, M. G. Hall, J. B. DeCoste and G. W. Peterson, *Nat. Mater.*, 2015, **14**, 512–516.
138 H. T. T. Nguyen, T. N. Tu, M. V. Nguyen, T. H. N. Lo, H. Furukawa, N. N. Nguyen and M. D. Nguyen, *ACS Appl. Mater. Interfaces*, 2018, **10**, 35462–35468.
139 M. V. Nguyen, H. N. Nguyen, T. A. Nguyen and K. M. Nguyen, *RSC Adv.*, 2022, **12**, 30201–30212.
140 Y. Chen, X. Zhang, X. Wang, R. J. Drout, M. R. Mian, R. Cao, K. Ma, Q. Xia, Z. Li and O. K. Farha, *J. Am. Chem. Soc.*, 2021, **143**, 4302–4310.
141 H.-X. Li, Z.-H. Zhang, Q. Wang, D.-X. Xue and J. Bai, *Cryst. Growth Des.*, 2020, **20**, 8015–8020.
142 J. Pang, S. Yuan, D. Du, C. Lollar, L. Zhang, M. Wu, D. Yuan, H. C. Zhou and M. Hong, *Angew. Chem.*, 2017, **129**, 14814–14818.
143 M. Zhang, Y. P. Chen, M. Bosch, T. Gentle III, K. Wang, D. Feng, Z. U. Wang and H. C. Zhou, *Angew. Chem.*, 2014, **126**, 834–837.